Experimental Study of Flow Boiling Heat Transfer Enhancement in Manifold Microchannel Heat Sinks for Air-assistant Water Flow

By

Niyam Bhandari

Submitted in Partial Fulfillment of the Requirements

for the Degree of

Master of Science in Engineering

in

Mechanical Engineering

YOUNGSTOWN STATE UNIVERSITY

August 2023

Experimental Study of Flow Boiling Heat Transfer Enhancement in Manifold Microchannel Heat Sinks for Air-assistant Water Flow

Niyam Bhandari

I hereby release this thesis to the public. I understand that this thesis will be made available from the OhioLINK ETD Center and the Maag Library Circulation Desk for public access. I also authorize the University or other individuals to make copies of this thesis as needed for scholarly research.

Signature:

Niyam Bhandari, Student Date

Approvals:

Dr. Kyosung Choo, Thesis Advisor Date

Dr. Jae Joong Ryu, Committee Member Date

Dr. Stefan Moldovan, Committee Member Date

Dr. Salvatore A. Sanders, Dean of Graduate Studies Date

Abstract

Heat sinks have played an integral part in the advancement of electronics, and the ever-evolving field means the production or development of even more efficient cooling methods are required. Heat sinks, generally consisting of small microchannels or minichannels, are constructed from a copper base providing a higher surface area and thermal conductivity thus providing a larger heat flux. Furthermore, an important aspect in large electronics cooling is the usage of liquid for cooling instead of the traditional air as the fluid. This would make for increased performance as liquids are much better at cooling than air. It is known that liquid cooling provides an efficient distribution of heat over more convection surface area (in the case of this research, a heat sink) than air would, allowing for higher power output. This would mean that if successfully implemented, the power output from higher end supercomputers and even massive machinery requiring successful cooling to perform tasks would be able to generate a better output than what is currently the trend. So, to help circulate the liquid, this research made use of a water block, and more importantly, a manifold water block which has channels running perpendicular to the channels on the heatsink. The third factor that plays a big part in this research is the phenomenon of flow boiling. The phenomenon whereby having a liquid that's close to saturation flow over a very hot source causing the liquid to boil and introduce vapor bubbles in the system has entranced fluid flow and heat transfer analysists for the past two decades. By incorporating all of these ideas into one research, the main goal was to identify the performance gain a manifold water block would have over a single-channel manifold water block which is commercially available used in cooling computer CPUs by measuring the heat flux for both the water blocks and trying to simulate flow boiling in the process. The experiment was also conducted to quantify whether air-assistant flow can increase the heat transfer performance in both manifold and single-channel manifold microchannel heat sink setup. The experimental findings agreed with what has been published in the literature namely by Dr. Kandilikar et. al where the introduction of manifolds increases the performance of a heatsink, so to further learn what role air bubbles play in the flow boiling process, a controlled air flow was introduced to the system and the results were observed via graphs. The graphs indicated that air-assistant flow had some effect on flow-boiling and thermal performance, but all of the results were within the margin of error for most cases. Furthermore, the addition of air to the flow in fact resulted in a lower heat flux while maintaining a higher wall superheat which is unfavorable.

Acknowledgements

First and foremost, I would like to provide a huge thanks to Dr. Choo for his continued support and expertise, as I would have been lost without his advice on my research. You pushed me to my limits and always believed in me, keeping my best wishes in your thoughts for which I am grateful. This research topic has been such a tough journey, but you have kept it fun and interesting for me, even at times when I was stumped and did not know where to go, for which I am highly appreciative of. I would also like to show my appreciation for Eric Haake, Dr. Stefan Moldovan, my peer, Mukesh Kalel, because without your valuable input on resin printing, data compilation, error analysis and slow-motion videography techniques, my research would be at a stalemate. I would also like to thank the Chemical Engineering laboratory and my friend José González García for helping me with the 3D printing process which was paramount for the success of my research.

Furthermore, this research would have been impossible without the help of Will Bevan, who has lent me a helping hand at every step of the way, being a mentor in the ways of performing heat transfer experiments involving fluid flow. You never thought of me as an annoyance and were always willing to stick around and help me figure out problems that arose even with your busy schedule so, thank you so much. Finally, I would like to thank my friends and family who showed me their love and support throughout my time at Youngstown State University.

Table of Contents

List of Figures

List of tables

Nomenclature

Variables

β	Volumetric quality (-)
D_h	Hydraulic diameter (µm)
W_{ch}	Width of channel (µm)
H_{ch}	Height of channel (µm)
k	Thermal conductivity (W/mK)
A/A_s	Cross-section Area (m^2)
ρ	Density (kg/m^3)
T	Temperature (°C)
x	Distance (mm)
$\dot{Q}_{cond}$	Heat flux via conduction (W/cm^2)
$\dot{Q}_{conv}$	Heat transfer via convection (W/cm^2)
h	Heat transfer coefficient (W/m^2K)
q^{n}_{max}	Critical heat flux for nucleate boiling (W/cm^2)
Q	Volumetric flow rate (GPH, L/m)
Re	Reynolds Number
R	Thermal Resistance (K/W)

q”	Heat flux calculated (W/cm^2)
V	Voltage (V)

Subscript

cond	Conduction
conv	Convection
ch	Channel
s	Surface
l	Liquid
g	Gas
∞	Surrounding fluid
max	Maximum
sat	Saturation
hs_{base}	Base of heat sink
Cu	Copper
tot	Total

Acronyms

HS	Heat sink
MCHS	Microchannel Heat sink

MMCHS	Manifold Microchannel Heat sink
CAD	Computer-Aided Design
CPU	Central Processing Unit
SD	Standard Deviation
SE	Standard Error
PTFE	Polytetrafluoroethylene
ONB	Onset of Nucleate Boiling
CHF	Critical Heat Flux
CNC	Computer Numerical Control

1 Introduction

Heat transfer enhancements have long been a topic that has intrigued researchers since the advancement of technology rose in the 60's. It could even be argued that the exponential evolution in electronics and technology in general was only achievable because of these heat transfer improvements. For example, comparing a 30-year-old desktop with today's technology, the method of heat transfer might be the same (usage of heat sink and forced convection via air), but the improvement is vast as today's computers have heat sinks that are a fraction of the size. Researchers applied better microchannels to heat sinks by optimizing the distance between each channel, the width, and the ratio of the width to the height for each specific application which made this leap in cooling possible. Similar to those researchers, additional enhancement of the heat sink cooling mechanism could be studied by virtue of two-phase fluid flow through different heat sink apparatus (such as a manifold microchannel heat sink) which could be further modified to fit specific electronic types in the future. This Chapter talks about the research objectives and a general outline of what this thesis entails to provide the readers with some grasp on the different concepts revolving around microchannel heatsinks, flow-boiling, and manifolds.

1.1 Research Objective

Understanding the mechanism of a heat sink and flow boiling is important as it helps develop new cooling methods for large computational machines and data centers. Using enormous cooling solutions prove ineffective and a cheaper and better alternative is always on the horizon which is why experiments on this topic have been improving with each iteration. Using the latent heat of the water vapors bubbles in conjunction with the manifolds can help researchers understand and improve this method of cooling. Following up on said research, this experiment investigates the effect of air-assisted flow boiling where the volumetric air quality changes from $\beta = 0$ to $\beta = 0.8$

to see if there is any effect on the heat flux and the wall superheat. β is defined as the volume fraction of air mixed in the fluid, which in this case is water, calculated using equation (6). Furthermore, a comprehensive understanding of flow patterns, anomalies with flow boiling, and pressure drops can also be determined for manifold microchannel heat sink when previous literature as well as this experiment are compared to each other.

This research was conducted as a supplement to future research on manifold heat sinks with flow-boiling where the parameters such as number of channels in the manifold, taper in the manifold, flow rate, and inlet temperature are changed, and it would be interesting to understand how air-assisted flow-boiling performs in those scenarios.

1.2 Thesis Outline

This paper starts by providing some basic overview on heat transfer enhancements such as methods other researchers have applied while also introducing readers to the research objective of this thesis. This chapter also talks about why heat transfer enhancements are so important and discusses the various parameters that might be involved when performing such experiments.

Chapter 2 starts off by providing some much-needed background on heat transfer mechanisms for a manifold heat sink such as conduction and convection while also delving into details about what classifies as a microchannel heat sink. The experimentation on air-assisted flow boiling in a manifold heat sink is a new concept taking into account the work done by previous researchers as outlined in Chapter 2 which talks about the past research done to create a manifold microchannel heat sink setup with the addition of volumetric air quality control as seen in research done by Rouse [1]. Chapter 3 outlines and goes in depth about the experimental setup as well as the equipment used for this research and data acquisition. Equipment used previously by Bevan [2] are talked about in depth and specific techniques and criteria for running the experiment successfully are also discussed in Chapter 3. Chapter 4 quantifies the research objectives through the use of charts and tables obtained through numerous hours of experimentation and data processing to explain the specific changes in the heat flux for air-assisted flow boiling in a manifold heat sink compared to regular flow boiling and flow boiling in an aftermarket computer CPU cooling unit.

Finally, Chapter 5 concludes the paper with some key findings from this research to clarify the results from this study.

2 Background and Literature review

2.1 Heat Sinks

Heat sinks are essential components when it comes to electronics cooling as with the use of electronics comes the drawback of heat generation. Without successful dissipation of this heat, the electronics bear a risk of malfunctioning mid operation which could range from mild damage to severe and catastrophic failure and even resulting in the loss of lives. So, now that heat dissipation has been established as an important aspect for electronics to function properly, the next topic is to discuss proper dissipation of the heat. Numerous methods have been used to perform the task of cooling electronics, but none have been quite as popular and widespread as heat sinks when it comes to cooling small sources of power such as a CPU, transistor, or a computer memory for example. Taking a heat source's excess heat and dissipating it into the surrounding is something heat sinks accomplish by the virtue of their large surface area compared to their size via the usage of microchannels. This is done by conduction where the heat sink absorbs the excess heat from the source and using forced convection, disperses it to the surrounding air. While heat sinks are effective on their own, forced convection along with the heat sink's own conduction has been proven to be much more effective at cooling computer CPUs and electronic components that generate a lot of heat.

Research conducted by Tuckerman and Pease in 1981 was one of the first of its kind where they proposed a design for a silicon-based Microchannel heat sink (MCHS), using integrated circuit fabrication techniques to fabricate channels that had an aspect ratio of 10:1 [3]. It wasn't until much later when Kandlikar et. al specified what can be categorized as a microchannel in his paper stating a hydraulic diameter of 10μm-200 μm of the channels can be classified as a microchannel. Dr. Kandlikar also elaborates about calculating the hydraulic diameter of the noncircular channel (rectangular, triangular, and trapezoidal channels) where it is stated that the hydraulic diameter could be written as four times the cross-section area to the perimeter as seen in equation (1) [4].

$$D_h = \frac{4W_{ch}H_{ch}}{2(W_{ch} + H_{ch})} \tag{1}$$

Since this thesis delves with heat sinks generally manufactured for use in CPU cooling, the material most commonly used to fabricate these MCHS is Copper because of its high thermal conductivity (398 W/mK) and relatively low density (8960 Kg/m^3). There are various techniques that can be used for the preparation of such microchannels, which is an important aspect for this research, and the industry standard for making the microchannel heat sink used in this research is CNC machining as specified on the manufacturer Bykski website. For specialized cases, such as for research purposes, other methods such as molding, milling and sawing, and waterjet cutting were prevalent while some manufacturing techniques such as printed circuit board and stereolithography were employed as stated by Kandlikar and Grande [4].

2.1.1 Conduction

Conduction, sometimes referred to as heat transfer by diffusion, is a phenomenon of heat transfer where the transport of energy occurs in a medium because of a temperature gradient, and the physical mechanism is carried out by atomic activity. This phenomenon can be observed in solids as well as fluids because conduction boils down to atomic movement i.e. collision and diffusion of random atomic and molecular motion in fluids and the migration of free electrons and lattice vibrational waves in solids [5]. Accordingly, heat transfer via conduction can be calculated by an equation originally developed by Joseph Fourier in 1822 [5] called the Fourier's law of heat conduction seen in equation (2).

$$\dot{Q}_{cond} = -kA\frac{dT}{dx} \qquad (2)$$

In equation (2), the $\frac{dT}{dx}$ refers to the temperature gradient, k is the thermal conductivity of the material, and A is the cross-section area. The negative sign in the equation is to indicate that heat is always transferred in the direction of decreasing temperature. For a more general statement of the heat conduction equation, equation (3) is presented, which accounts for variable thermal conductivity as well as the rectangular space coordinate.

$$\left(\frac{\partial}{\partial x}\left(k\frac{\partial T}{\partial x}\right) + \frac{\partial}{\partial x}\left(k\frac{\partial T}{\partial y}\right) + \frac{\partial}{\partial x}\left(k\frac{\partial T}{\partial z}\right)\right) + \dot{q} = \rho C_p\frac{\partial T}{\partial t} \qquad (3)$$

Factoring out the transient state of equation (3), and considering a one-dimensional case, the heat conduction equation can be rewritten as seen in equation (4) [5].

$$\dot{Q}_{cond} = kA\frac{(T_1 - T_2)}{\Delta x} \qquad (4)$$

2.1.2 Convection

The second method of heat transfer this paper will discuss is convection. Convection refers to the process of heat transfer through a fluid via bulk or gross motion of fluid particles [5]. Under convection, there is free and forced convection, where free convection refers to the natural motion of the fluid while forced convection refers to the usage of an external source to propel the fluid, such as using a fan or a pump, across a channel or surface. Furthermore, there is also the classification of internal and external convection, where internal convection means flow through a pipe or closed ducts whereas external convection means fluid is pushed to flow across a plain surface. For this paper's intents and purposes, using Newton's rule of cooling, the rate of convection heat transfer can be stated as a function of temperature difference as seen in equation (5), with h being the heat transfer coefficient, A_s being the cross-section area heat transfer is occurring, and T_s is the surface temperature, while T_∞ being the temperature of the fluid in the surrounding appropriately far from the surface.

$$\dot{Q}_{conv} = hA_s(T_s - T_\infty) \tag{5}$$

2.2 Flow Boiling

The phenomenon of flow boiling is of particular interest in the field of electronic cooling. Water has already been eclipsing the market of cooling for a decade since newer electronics are using more power to do more work and as a result producing more heat. While modern air coolers with their forced convection are effective, they pale in comparison to their water-cooling counterparts because of the higher density and an overall better capability to whisk heat away from sources while remaining less audible than air coolers. This clearly indicates water being a better coolant when using forced convection than air. Thus, using water as a medium for forced convection and cooling massive electronics that generate a lot of heat would be much more effective. Flow boiling assists in this specific case as with flow boiling, there exists two phases: water and air bubbles formed from the boiling from water which in turn increases the heat flux of the cooling unit. With the increase in the critical heat flux (q^{n}_{max}) for nucleate boiling, there would also be an increase in the cooling efficiency of the cooling unit. Since boiling has the added benefit of dissipating large quantities of heat by virtue of its latent heat potential according to Kalani and Kandlikar [6], incorporating it to maintain a low temperature for heat sources has been well studied and a brief literature review goes into detail the characteristics of flow boiling with microchannel heat sinks and manifolds. Two boiling curves showing the heat flux with respect to the wall superheat ($T_{ch\_base} - T_{sat}$) can be seen in Figure 2-1 Figure 2-2 and which will provide further context on the phenomenon of boiling.

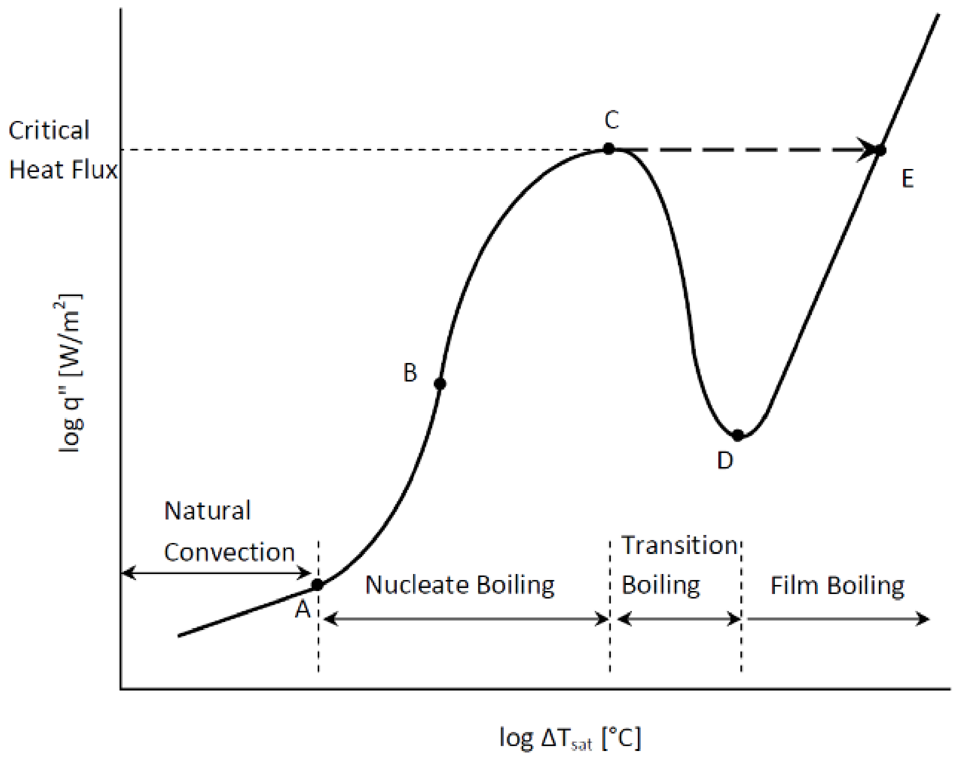

Figure 2-1: Boiling curve [5].

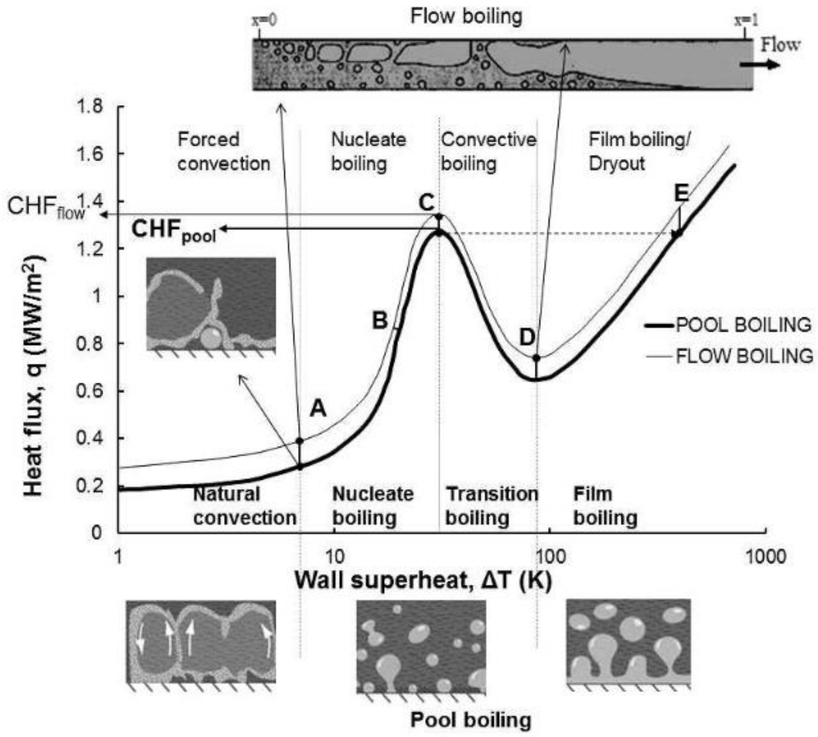

Figure 2-2: Flow boiling and pool boiling curves with nucleate boiling visualization [7].

The boiling curve shows heat flux which is the rate of heat transfer per unit area on the Y-axis while wall superheat which is the temperature difference between the surface temperature and the saturation temperature of the liquid used is denoted on the X-axis. First identified by Nukiyama [8], Figure 2-4 shows that there are various flow regimes when a fluid undergoes pool boiling starting from natural convection after which there is a sharp rise in the heat flux and a moderate increase in the wall superheat which continues till Critical Heat Flux (CHF) is reached. This entire region is called the nucleate boiling regime because of the formation of vapors bubbles in the liquid due to boiling. After CHF is attained, the fluid undergoes a drastic decrease in heat flux while the wall superheat continues to increase after finally reaching the end of transition boiling after which the heat flux rises along with the wall superheat as a linear function [5].

The phenomenon of boiling is visible to the naked eye where the liquid comes into contact with a surface or source kept at a temperature that is sufficiently higher than the liquid's saturation temperature causing a liquid to vapor transition. At the interface where the surface and liquid come into contact, vapors bubbles can be seen being generated quickly which when of a specific size, separate from the surface and because of its lower density as a gaseous entity, makes it way to the liquid's free surface. Flow boiling adds another dimension to the phenomenon of boiling as with the addition of forced convection comes the added advantage of higher heat transfer coefficient and better performance especially in microchannel heat sinks. There are also multiple boiling regimes when flow-boiling occurs in microchannels with each case having its own flow pattern which is visualized in Figure 2-4. This change is brought upon by the increase in heat supplied to the microchannel base causing more vapors to accumulate inside the channels causing a change in the flow regime. Research done for flow-boiling at low flow rates (0 to 61.5 mL/min) for a microevaporator 198 × 241 µm microchannel by Elmer [9] provides more insight on how ONB causes higher heat fluxes.

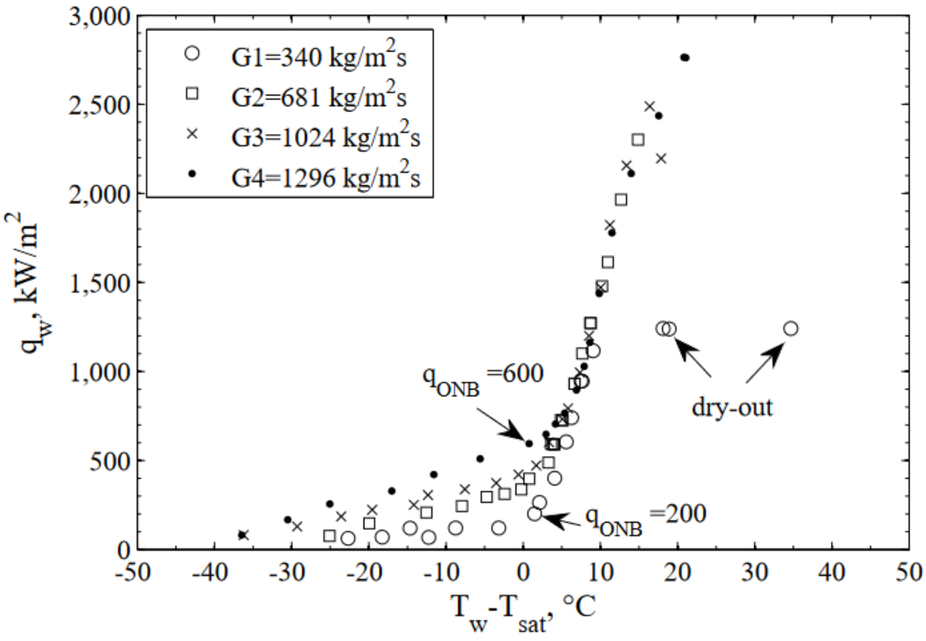

Figure 2-3: Boiling curves for microevaporator 198 × 241 μm microchannel at different mass fluxes [9].

Figure 2-3 shows that ONB is the point where there is a sharp increase in the heat flux compared to the wall superheat. The point at which ONB occurs also depends on the mass flux as higher mass flux tend to reach ONB at lower wall superheat, generally before the saturation temperature of the fluid (ultra-pure water) is reached as demonstrated by the data points for G3 and G4 from the figure above.

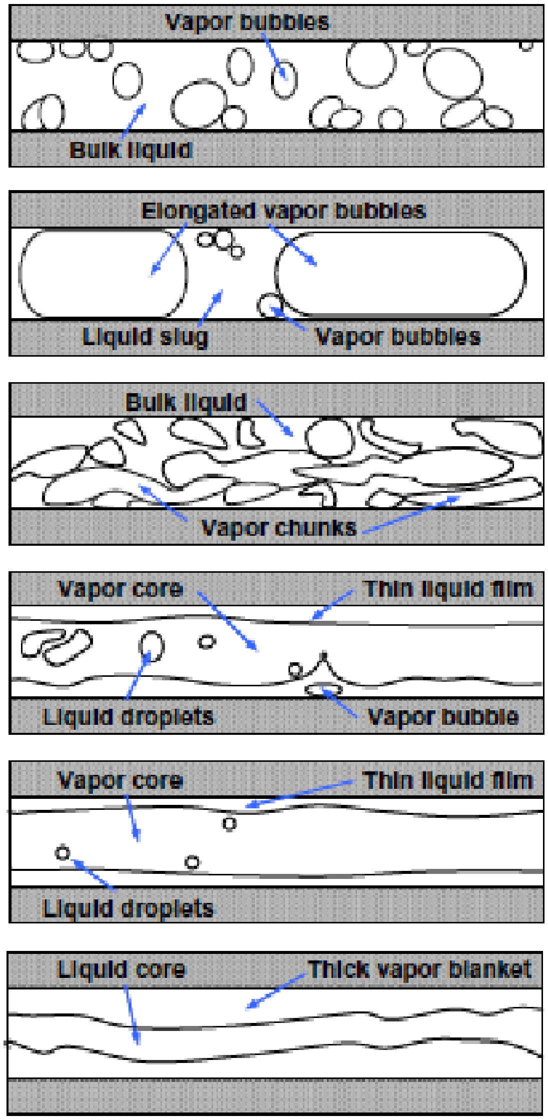

Figure 2-4: Flow boiling regime schematic in microchannels [10].

Despite the advantages of flow-boiling to dissipate high heat fluxes, experimental investigations using flow-boiling in microchannels as a cooling apparatus suggest that the performance for microchannels using flow-boiling have significantly reduced performance compared to theoretical and numerical simulations if no heat transfer enhancement techniques are employed. Flow instabilities, reverse flow, and fluctuations in the pressure drop are identified to be the cause of this performance drop when using flow-boiling as a cooling mechanism with a better visual demonstration of this phenomenon in Figure 2-5 [11].

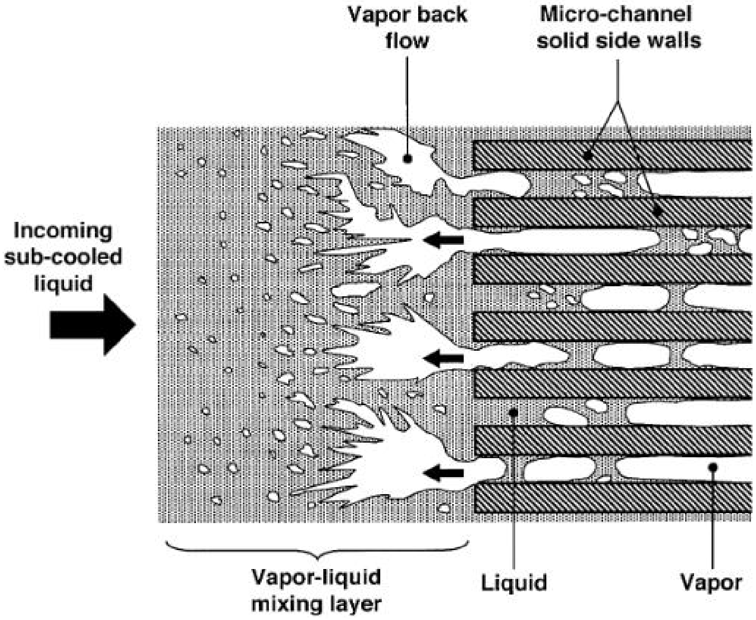

Figure 2-5: Schematic visualization of observed backflow at high heat flux [11].

In microchannels, the presence of large vapors in the cross-sectional area of the channels itself reduces the liquid film thickness near the heated channel walls leading to dryout. To increase the heat transfer capabilities of these channels, removal of vapors to keep the channels filled with liquid is essential as this effectively extends the point where CHF can occur [12]. Using this insight, Kandlikar et al. [13] introduced artificial nucleation sites as well as added an inlet restrictor to stabilize the flow, this in turn led to a significant drop in pressure fluctuations and a stable flow was achieved albeit obtained at low heat fluxes. Furthermore, another study by Mukherjee and Kandlikar [14] concluded that reverse flow in microchannels occur due to pressure built up in the channels from rapid bubble growth. They did this by numerically simulating a nucleating bubble in a channel and studying the effect of inlet restrictors. So, adding a manifold design waterblock could provide more area for the bubble to rise up to leaving the channels unblocked and thus prolonging CHF as well as reducing pressure drop which will be discussed in the next sub section.

2.3 Manifolds-microchannel design

Manifolds-microchannel design has been an extensively studied topic in the field of thermal management because of its ability to dissipate great amounts of heat in high power electronics and it has been closely researched for several years. First proposed by Harpole et al [15], manifolds provide more surface area for an effective heat transfer while lowering the pressure drop by virtue of its channels above the MCHS placed orthogonal to the MCHS' length. Effectively, half of the manifold channels work as inlet while the other half act as outlet channels alternating along the length of the microchannel [16]. A diagram depicting the workings of the manifold MCHS showing its simplest geometry can be seen in Figure 2-6.

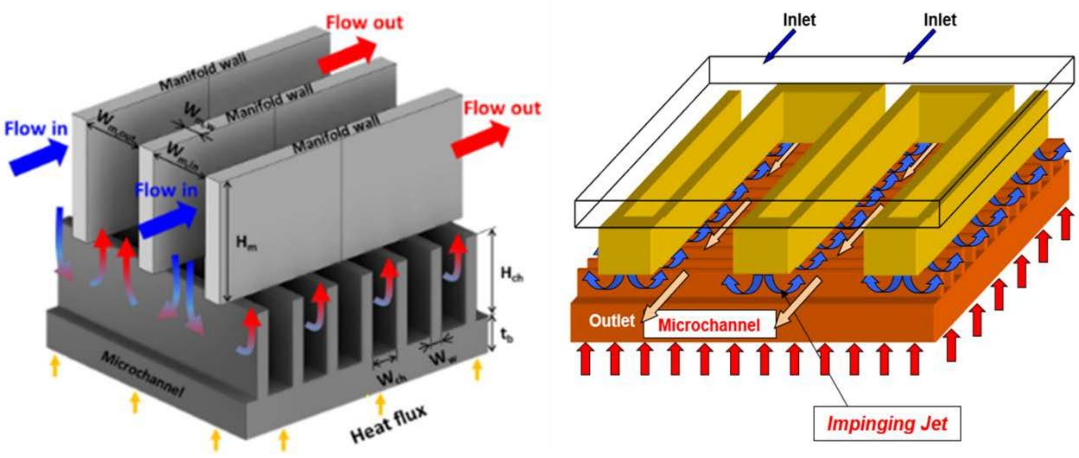

Figure 2-6: Schematic showing how manifold microchannel heat sink work [16], [17].

As seen in Figure 2-6, half of the manifold channels work as inlets and the other half work as outlets with the inlets supplying cold fluid which impinges down to the microchannel and after circulation goes back to the manifold outlet channels completing the cycle. Research interest in this field has been increasing rapidly as the working fluid is forced down causing a collision from the manifold channels to the microchannels of the heat sink creating thin thermal boundary layers due to jet impingement improving heat transfer performance. Incorporation of manifolds in MCHS also means that less pumping power is required as a factor of the large cross-section area of the manifolds shortening the flow path of the fluid through the microchannels as well as the jet impingement come into effect [16].

One study by Kalani and Kandlikar [6] evaluated the pressure drop in a microchannel heat sink using uniform and tapered manifolds as seen in Figure 2-7 and Figure 2-8 where they show that adding tapered manifolds can be beneficial to reducing the pressure drop during flow boiling.

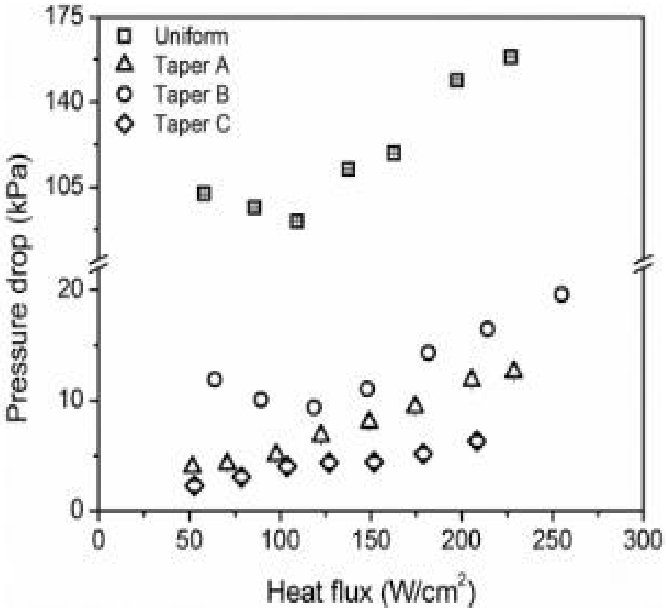

Figure 2-7: Pressure drop performance of plain chip with different manifold configurations [6]

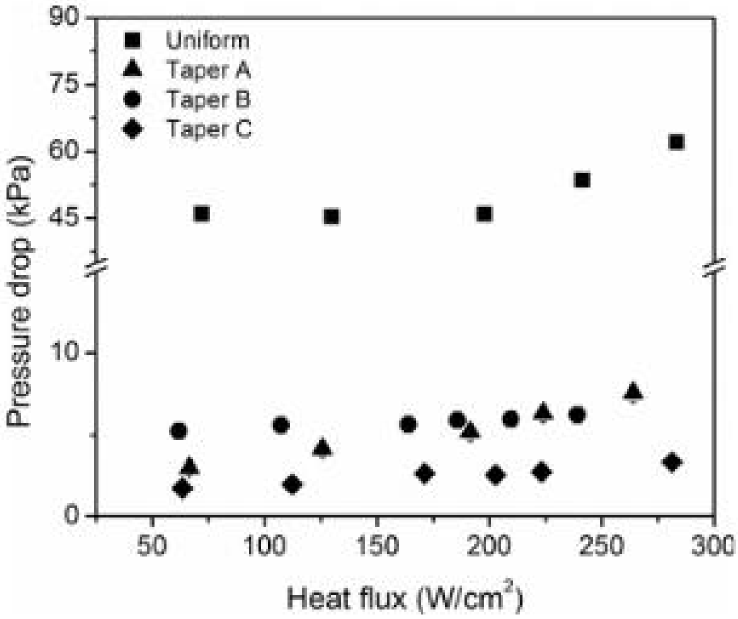

Figure 2-8: Pressure drop performance of microchannel chip with different manifold configurations [6]

Furthermore, as discussed earlier manifolds also provide a superior thermal performance compared to a conventional MCHS because of the jet impingement creating of thin thermal boundary layers and these effects have also been heavily studied at lower fluid flow rates.

2.4 Air-assistant two-phase flow

Normally during flow-boiling, there is already two-phase flow going on with the vapor bubbles generated from the fluid reaching its saturation temperature mixed with the flow. Furthermore, researchers have found that adding gas to a liquid only impinging jet enhances the heat transfer rate. Therefore, addition of air to a flow-boiling experiment should theoretically increase the heat transfer rate of the overall system. In a study conducted by Zumbrunnen and Balasubramanian [18], there was an observed increase in the heat transfer rate of liquid-only impinging jets by a factor of 2.2 when the volumetric fraction was between β values 0 - 0.86 and when the Reynolds number was between $3700 \leq Re_w \geq 21{,}000$. Another study conducted by

Serizawa et al. [19] also found a similar result where the heat transfer coefficient increased by a factor of two when studying circular jet with an air-water mixture this time with a fixed volumetric fraction of $\beta = 0.53$ while changing the Reynolds number from $25{,}000 \leq Re_w \geq 125{,}000$. These results show that experimentally, addition of gas into a liquid only jet increases the heat transfer properties of the overall system. A visual representation of air-assistant fluid flow through a nozzle for various β can be seen in Figure 2-9.

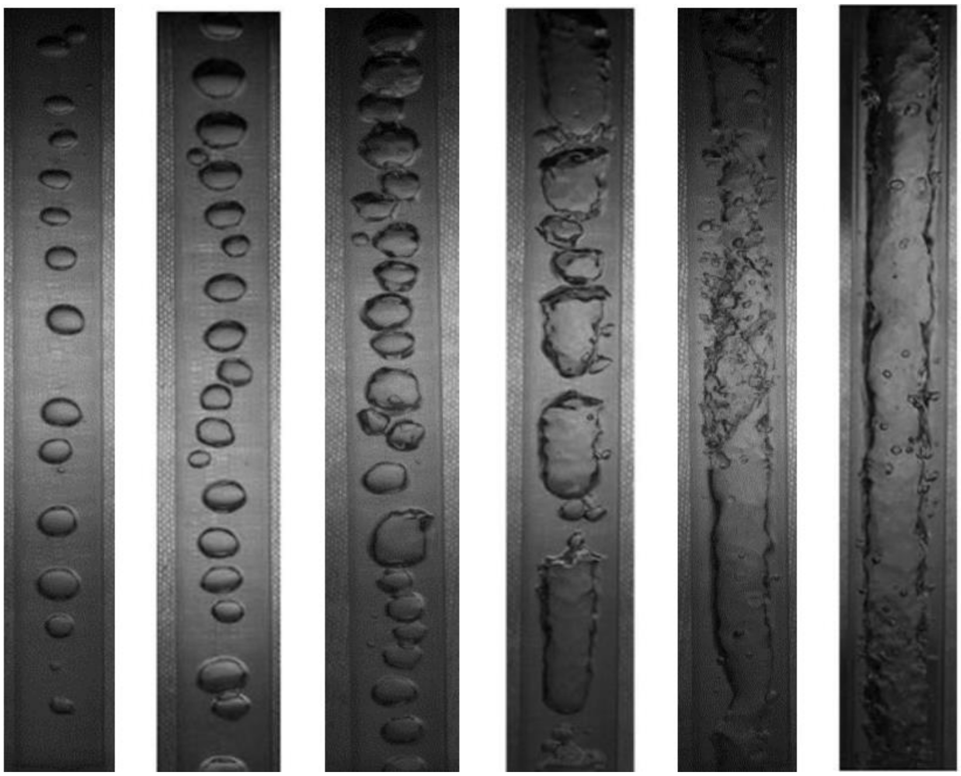

(a) $\beta = 0$ (b) $\beta = 0.2$ (c) $\beta = 0.3$ (d) $\beta = 0.6$ (e) $\beta = 0.8$ (f) $\beta = 0.9$

Figure 2-9: Two phase flow patterns inside a nozzle for different β [20].

The volumetric fraction of air β was calculated using the equation (6) where Q_g and Q_l are flow rate of gas and liquid respectively:

$$\beta = \frac{Q_g}{Q_g + Q_l} \tag{6}$$

This equation was used to derive the flow rate for air when the water flow rate was fixed at 10 GPH and 6 GPH which has been tabulated in Table 4-2 and Table 4-3. Manipulating the equation for a known β could easily provide the air flow rate required to maintain a specific β when the water flow rate is fixed as well which is given by:

$$Q_g = \frac{Q_l \beta}{(1 - \beta)} \tag{7}$$

Finally, using equation (7), the air flow rate was calculated for a fixed β when the flow rate of water was kept at 10 GPH and 6 GPH respectively.

3 Methodology and Experimental Setup

The experimental work required for this research was done in parts with the first part being the procurement of a plate fin microchannel heat sinks that was readily available off the shelf or on an online shopping platform. While the experimental setup is closer to the ones used by Kalani and Kandlikar [6], [21], this experiment is also considering the air flow rate controller setup like Rouse [1] to make sure there is air-assisted flow boiling during experimentation. While not exactly following Dr. Kandlikar's setup with a pressure transducer to measure pressure drop and a condenser, this experimental setup has been verified with a study on pool boiling to ensure the accuracy and validity of the results.

3.1 Fabrication of Manifolds

Water blocks generally used in desktop cooling utilize acrylic or plexiglass because of its thermal resistance capabilities. They also offer transparency to understand the flow mechanism of a water-cooled unit along with decent strength and resistance to erosion or degradation over time. Several research involved the use of manifold MCHS because of its intricate morphology in cooling electronics by making use of machining [22]–[24], microfabrication [25]–[27], and additive manufacturing technology [28]. So, using these literatures as a starting point, the first technique to be utilized was machining where acrylics were purchased to be machined but because of unsuccessful attempts to machine the acrylic with the equipment on hand, the research moved on to using 3D printed resin which offered similar characteristics without much compromise.

The 3D printed resin was printed using the Formlabs 3D printer as seen in Figure 3-1 used a special heat resistant resin (High Temp V4) also manufactured by Formlabs as this resin could withstand temperatures of up to 210°C and was translucent enough to visualize the mechanism during the experiment. With the material selected, a model needed to be sketched out with a manifold design to go on top of the heat sink apparatus for the flow-boiling experiment.

Figure 3-1: FormLabs 3D printer.

This was done using the commercially available Computer-Aided Design (CAD) software SolidWorks where a rough dimension of the heatsink was taken and translated into SolidWorks and based on the measurements from the heatsink and the single channel manifold water block combination, a preliminary plain model with coarse manifolds was created. This was necessary to ensure the heatsink fit on the 3D printed part. Then, a proper manifold design was created on the surface that was to be in contact normal to the microchannels of the heatsink to encompass all the channels as seen in Figure 3-2. This made sure the fluid travelled along the length of the manifold before impinging onto and after circulation throughout the microchannels. This is essential as this travelling and impinging onto the channels is the driving force for a higher heat flux for this apparatus. Once the 3D print was completed, the resin was washed in alcohol and cured with the heatsink fitted onto the manifold design to ensure no shrinkage occurred in the part. The part used for washing and curing the 3D printed part can be seen in Figure 3-5 (a) and (b) respectively. Finally, after the curing process, the part was tapped using uxcell a15012200ux0336 ¼ - 19 BSP pipe thread purchased from Amazon to have the fittings on for experimentation which is pictured in Figure 3-6.

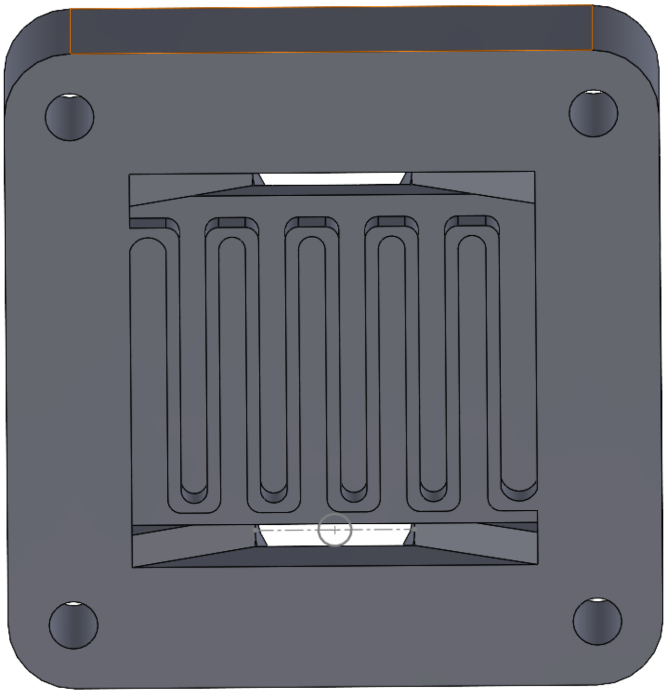

Figure 3-2: SolidWorks model of the manifold water block.

The model was created after taking the dimensions of the heat sink as well as the waterblock created by the manufacturer Bykski. The manifold water block were modelled to have a channel gap of 2 mm with the thickness of the channels being 1 mm, but the final 3D print had some shrinkage due to curing resulting in the channel gap being 1.7 mm and the width of the channel reduced to 0.6 mm. The heat sink and its dimensions can be seen in Figure 3-3. Following the dimensions of the heat sink, the waterblock going on top of the heatsink was also measured to model the manifolds after. This gave a rough idea on the manifold waterblock's design leading to the SolidWorks model in Figure 3-2.

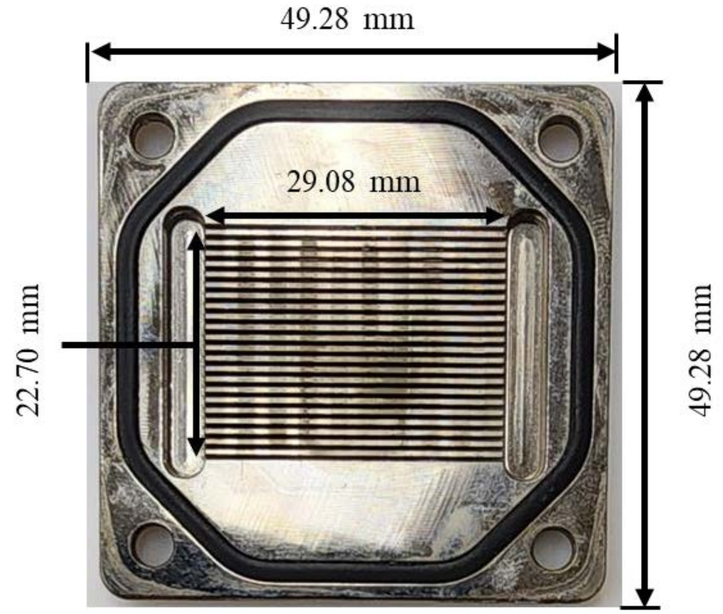

Figure 3-3: Heat sink from manufacturer Bykski with dimensions.

One thing to note from Figure 3-3 is that while the shape of the heat sink is square, the area over which the channels were spread out was not and this area was crucial to model the manifold area as well. Furthermore, using AutoCAD to approximate the channel width and height to calculate the hydraulic diameter, it was found to be 0.638 μm which can still be regarded in the microchannel regime.

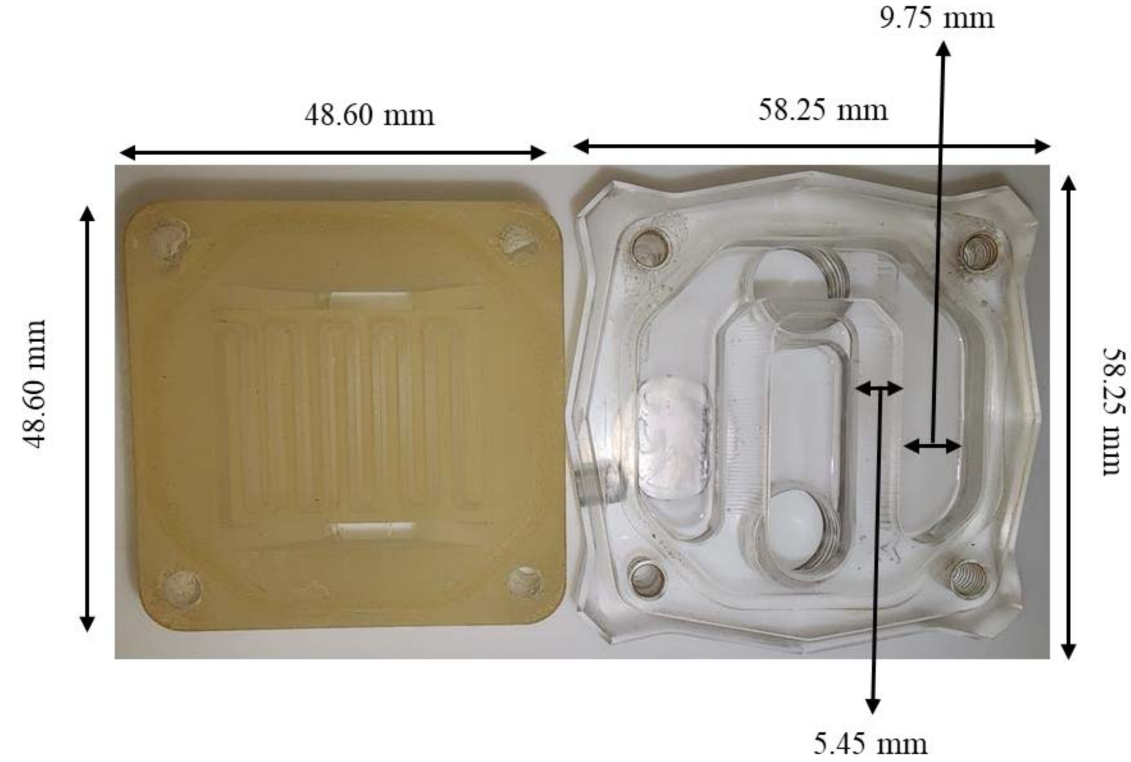

Figure 3-4: 3D printed resin waterblock compared to the manufacturer provided waterblock.

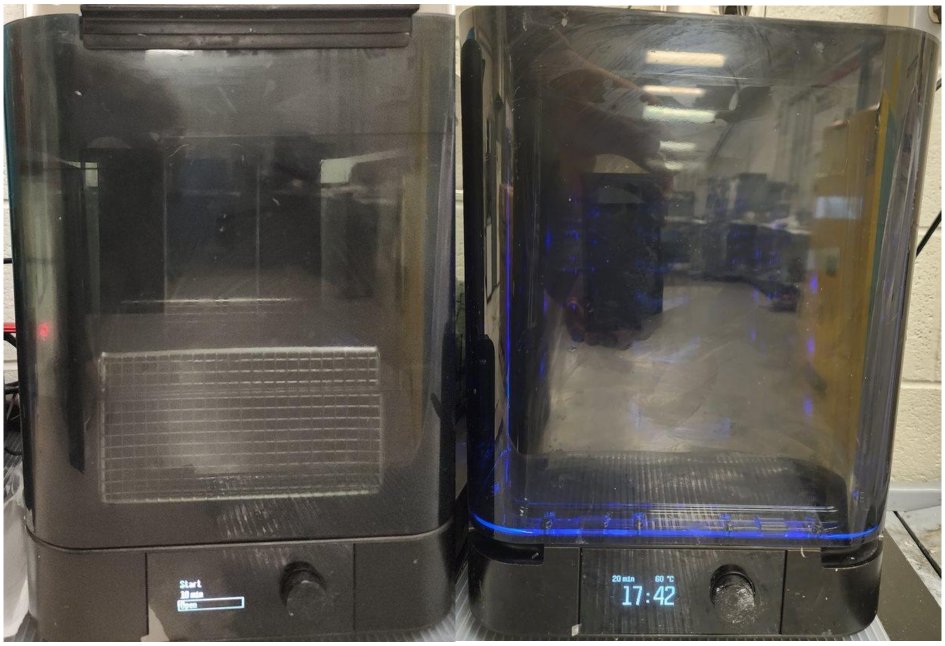

(a) (b)

Figure 3-5: Machines used for washing excess resin and curing the resin print.

Figure 3-6: uxcell G ¼ - 19 BSP pipe thread.

3.2 Flow Apparatus

The flow apparatus for this research is comprised of a few items, the first of which is the hot temperature bath model name Polystat PN-10124-20 by Cole-Parmer as pictured in

Figure 3-7 which provided a constant flow of water to the flow-boiling unit. From the manufacturer's website, the hot temperature bath had a temperature range of 10-200℃ and a maximum pumping power of 11 L/min meeting the requirements for this research. The outlet of the temperature bath unit was connected using flexible tubing to a Dwyer flow meter (RMB-84-SSV) with a flow range of 0-40 GPH which can be seen in Figure 3-8 and the outlet of this flow meter was connected to the inlet of the manifold microchannel heat sink whereas the outlet of the manifold microchannel heat sink was connected to the inlet of the constant temperature water bath completing the loop.

Figure 3-7: Cole-Parmer Polystat hot temperature circulating bath.

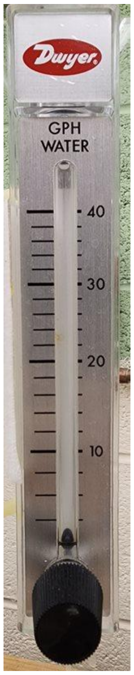

Figure 3-8: Dwyer variable flow meter.

To introduce air into the apparatus, two Omega mass flow controllers (FMA5400A/5500A) were used as pictured in Figure 3-9 to provide a constant air flow rate between 0 to 2500 mL/min for the air-assisted flow boiling experiments. For this setup, a Y-fitting was added to the previous apparatus where one of the tube supplied a constant 10 GPH of 90℃ water while the other tube supplied a constant air flow rate based on the volumetric air quality β before they mixed in the pipe connected to the manifold microchannel heat sink.

Figure 3-9: Omega Air mass flow controller.

3.3 Heater Apparatus

The driving source for this experiment is the heater apparatus setup previously manufactured and implemented by Will Bevan in the Heat Transfer lab at Youngstown State University. According to Bevan, the design was based around three major criteria: minimal heat loss to the surrounding, practicality of data acquisition, and modular capabilities [2].

The heater apparatus consists of a copper base block with a housing for six Tutco CH43810HW cartridge heaters and a copper section atop the base block that accommodated two K-type thermocouples spaced 20 mm apart from each other. These thermocouples allow for enough temperature data acquisition required for the calculations of results in this experiment. At the absolute surface is the copper plate which makes contact with the manifold minichannel heatsink that is forced into position using a clamp and two rubber bands for added stability. Bevan used PTFE Teflon as the insulating material to enclose the copper heater ensuring minimal heat loss because of Teflon's low thermal conductivity and high melting point making it suitable for high-temperature application. Figure 3-10 shows a schematic of entire heater block and Figure 3-11 shows the fully assembled heater apparatus setup.

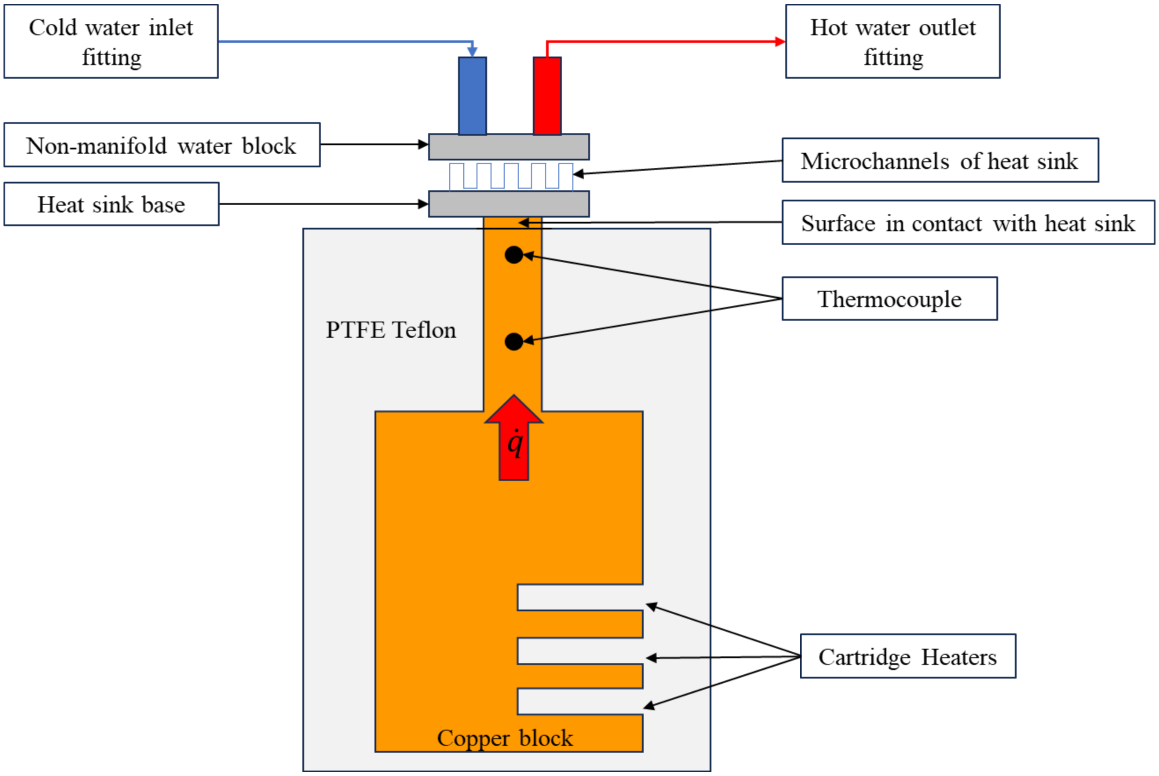

Figure 3-10: Heating apparatus setup layers visualized.

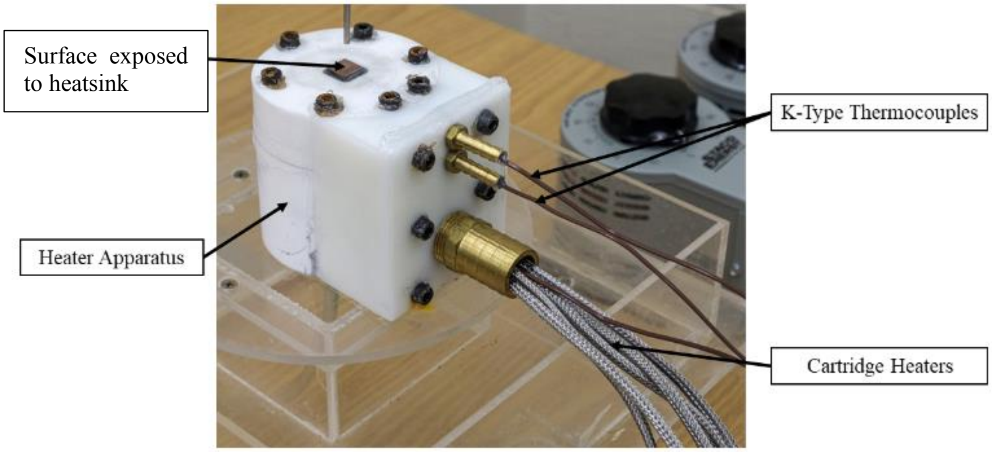

Figure 3-11: Assembled heat apparatus [2]

Powering this source were two variable transformers which could be used to regulate the energy being supplied to the cartridge heaters. These variable transformers were manufactured by

Staco Energy Products with the model number 3PN10101B. The transformers require an input voltage of 120V and provide a variable output voltage ranging from 0 to 140V while the current remains constant at 10 Amps.

The temperatures were recorded by the aforementioned K-type thermocouples in real time by using the Omega OM-CP QuadTemp2000 temperature data recorder pictured in Figure 3-13. The thermocouples were connected to the data recorder and the latter was then connected to a laptop for data acquisition. Figure 3-12 shows the Staco Variable Transformers while Figure 3-13 shows the Omega Temperature Data Recorder respectively.

Figure 3-12: Staco variable transformers.

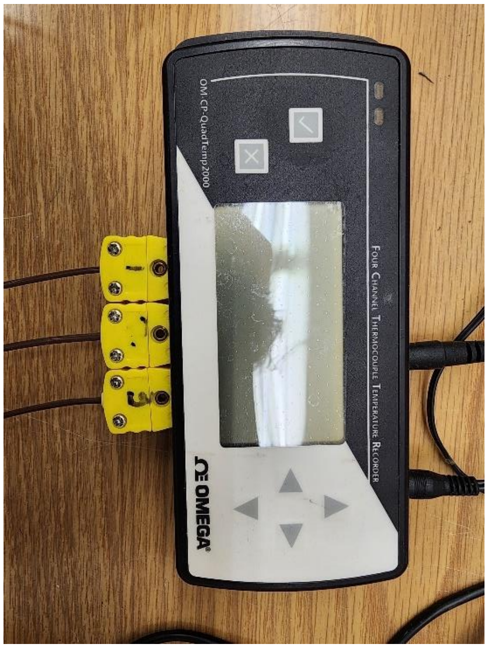

Figure 3-13: Omega OM-CP QuadTemp2000 Temperature recorder.

Using the temperatures recorded using the Omega OM-CP Temperature recorder, the temperature gradient necessary to calculate the effective heat flux was calculated using equation (8).

$$\frac{dT}{dx} = \frac{T_1 - T_2}{x} \quad (8)$$

T_1 and T_2 are the temperature recorded by the thermocouple respectively with T_1 recording temperatures closer to the base of the copper block while T_2 recorded the temperature of the copper block closer to the surface where the heat sink contacted the copper block. The distance between the two thermocouples were measured using a digital caliper and it is denoted by x.

The heat flux was then calculated using the one-dimensional heat transfer equation given by Fourier's Law, which was indicated in equation (2), using the following equation

$$q'' = -k_{Cu}\frac{(T_1 - T_2)}{x} \tag{9}$$

In equation (9), k_{Cu} is the thermal conductivity of copper in W/cmK and q'' is the effective heat flux. Next, the surface temperature of the heat sink base was calculated via extrapolation and using the total thermal resistance from the copper block to the surface of the heat sink and the heat flux and the equation for the surface temperature is given by equation

$$T_{hs_{base}} = T_1 - q'' A\, R_{tot} \tag{10}$$

Here, A is the area of the copper block surface in contact with the heat sink base and R_{tot} is the total thermal resistance from thermocouple 1 to the base of the heat sink calculated using the thermal resistance model pictured in

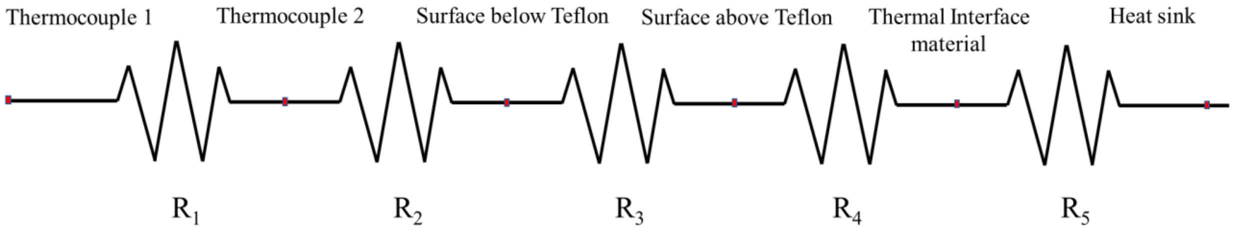

Figure 3-14: Resistance model used to calculate total thermal resistance.

The total resistance R_{tot} was calculated by adding all the resistances and each resistance was calculated using the following equations respectively.

$$R = \frac{L}{kA} \tag{11}$$

$$R_{tot} = \frac{L_1}{k_{Cu}A_{Cu\,block}} + \frac{L_2}{k_{Cu}A_{Cu\,block}} + \frac{L_3}{k_{Cu}A_{Cu\,block}} + \frac{L_{TIM}}{k_{TIM}A_{Cu\,block}} + \frac{L_5}{k_{Cu}A_{HS}} \tag{12}$$

In equation (11), L is the length between two quantities, so for R_1, L would be the length between two thermocouples which was 20 mm, k is the thermal conductivity of copper, and A is the cross-section area of the surface.

3.4 Procedure

To start off the experiment, the flow rate was chosen to be 10 GPH/0.6309 LPM to ensure that flow boiling was observed. Another water flow rate of 6 GPH/0.3785 LPM was used to compare the trend between the two flow rates which followed the exact steps as used for the experiment when ran at 10 GPH. A lower flow rate meant that the flow had ample time to make contact with the manifold minichannel heatsink meaning the flow could properly take heat away from the heatsink using flow boiling. To introduce air to the setup, a Y-connector was plugged with one end connected to the outlet of the mass flow controller while the other end was connected to the outlet from the Dwyer flowmeter.

The procedure for air-assisted flow boiling experiments is as follows. First, the Cole-Parmer Polystat hot temperature circulating bath was turned on and set to 90°C. This temperature was set below the boiling point of water to allow for flow boiling to occur while flowing in the heatsink apparatus. Once the temperature reached 90°C, the inlet and outlet for the manifold microchannel heatsink were connected and the heatsink apparatus was placed on top of the copper heat source. A thin layer of thermal interface material produced by Therma grizzly called the Kryonaut was applied at the contact point to ensure efficient thermal transfer from the copper heat source to the baseplate of the heat sink. Thermal grizzly's Kryonaut was chosen because of its high thermal conductivity compared to its competition at 12.8 W/m*K. With the thermal paste applied, the heat sink apparatus was clamped on to the copper heat source and the top and bottom sides of the heat sink apparatus was held down further using rubber bands. The two Staco Energy variable transformers were turned on and the applied heat flux was increased to the required voltage that the experiment is to be performed at. The temperature data was taken once a steady state occurred which meant that a temperature variation of ±0.8°C occurred over a time frame of 10 minutes. The air flow rate was increased based on the volumetric air quality calculation ranging from $\beta = 0.1$ to $\beta = 0.8$ and the temperature data was taken accordingly. Once all the data points for a particular setup (manifold or single-channel manifold) was taken, the configuration was switched out to the setup that has yet to be measured. A flowchart visualized in Figure 3-15 provides a more graphical representation of the experimental procedure. This process was done till a set of temperature data ranging from a measured voltage of 22.45 V to 44.785 V was obtained.

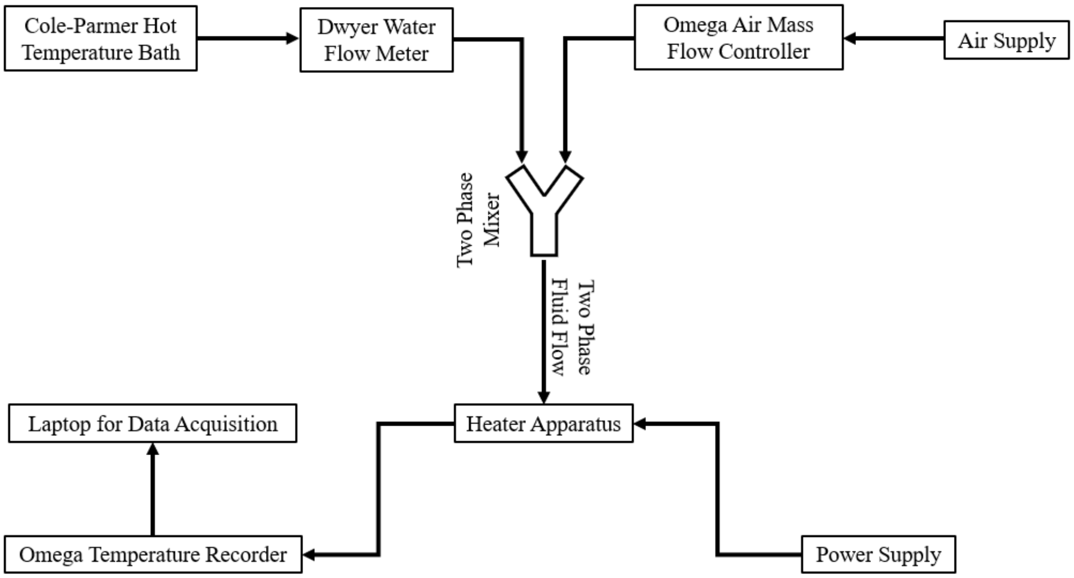

Figure 3-15: Schematic of flow-boiling experiment apparatus.

4 Results and Discussion

4.1 Uncertainty Analysis

Uncertainty exists in all experiments be it from bias, instrument, or even human error. To mitigate this and provide readers an accurate assortment of results from experiments, an in-depth uncertainty analysis is instrumental. Thus, for this experiment, an uncertainty analysis on all the major quantities derived was performed. Following the error analysis packet provided by the Mechanical Engineering Department at Youngstown State University [29], the standard expression for relative uncertainty that propagates from each independent variable x_i to y is defined by e_i seen in equation (13):

$$u_i = \frac{\partial y}{\partial x_i}|_{x_i = \bar{x_i}} u_{x_i} \tag{13}$$

The bias uncertainty in the experiment was measured by sensor calibration procedures while the precision errors of the data acquisitioned were evaluated by multiplying the standard deviation of the sample data by the student t-factor to account for the difference in data within a 95% confidence interval.

The relative uncertainty of the temperature of the base of the heat sink was derived as follows:

$$e_{T_{HS_{base}}} = \sqrt{\left(\frac{u_{precision_{T_1}}}{T_1}\right)^2 + \left(\frac{1}{T_1 - R_{tot} q^{"} A} \left(-R_{tot}\, A\right)\right)^2 u_{q^{"}}^2 + \left(\frac{1}{T_1 - R_{tot} q^{"} A} \left(-R_{tot}\, q^{"}\right)\right)^2 u_A^2} \tag{14}$$

Similarly, the relative uncertainty of the effective heat flux was also calculated given below

$$e_{q^{"}} = \sqrt{\left(\frac{u_{precision_{T_1}}}{T_1}\right)^2 + \left(\frac{u_{precision_{T_2}}}{T_2}\right)^2 + \left(-\frac{res\ error}{2d}\right)^2} \tag{15}$$

A detailed derivation of the uncertainty associated with the temperature and the heat flux as well as all the independent terms that the aforementioned terms are dependent on is done in Appendix B.

Finally, the results of the uncertainty analysis was tabulated and shown in a table below.

Table 4-1: Uncertainty analysis

Measured/Calculated Terms	Uncertainty associated	Max relative uncertainty	Max total uncertainty
T_1 (°C)	e_{t_1}	0.01663	4.02352
T_2 (°C)	e_{t_2}	0.01658	2.67136
x (mm)	e_x	0.00025	0.00500
A (mm^2)	e_A	0.00418	0.00707
q"(T) (W/cm^2)	$e_{q''_T}$	0.00037	0.05945
T_{HS} (°C)	$\boldsymbol{e_{t_{HS}}}$	**0.01664**	**2.02503**
q" (W/cm^2)	$\mathbf{e_{q''}}$	**0.03308**	**5.35882**

One thing of note is that the uncertainty associated with T_1 is much higher than that of T_2 or T_{HS} which is because T_1 measures the temperature of the thermocouple near the source meaning it is at a much higher temperature than thermocouple 2 placed near the surface or the base of the heat sink. The temperature for T_1 is almost 100°C higher for some cases leading to such a high uncertainty associated with T_1.

4.2 Results for flow-boiling at water flow rate of 10 GPH

At a water flow rate of 10 GPH,

Table 4-2 provides an insight on the air flow rate that is required to achieve a specific β.

Table 4-2: Volumetric air quality when water flow rate is 10 GPH.

	0.1	0.2	0.3	0.4	0.5	0.6	0.7	0.8	0.9
Water Flow Rate (gph)	10	10	10	10	10	10	10	10	10
Air Flow Rate (gph)	1.11	2.50	4.29	6.67	10.00	15.00	23.33	40.00	90.00
Air flow rate (mLpm)	70.1	157.7	270.3	420.6	630.9	946.3	1472.1	2523.6	5678.1

With the help of this table, the air flow rate can be specified during experimentation on the Omega mass flow controller when the water flow rate is at 10 GPH. From this, a few results were extrapolated which can provide insight on the effect of volumetric quality on flow-boiling at 10 GPH water flow rate.

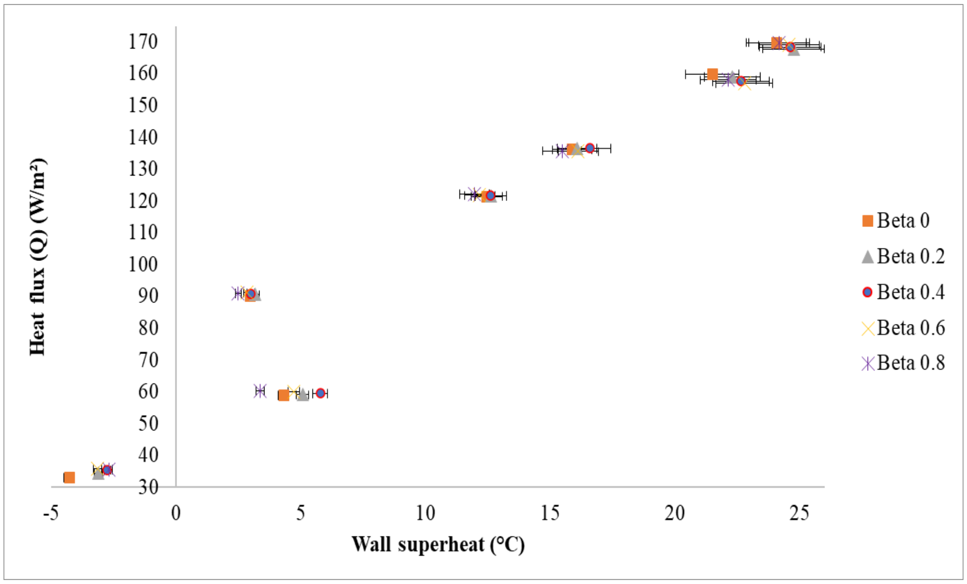

Figure 4-1: Plot showing the wall superheat as a function of heat flux for single-channel manifold microchannel heat sink setup.

Figure 4-1 shows the trend of increasing wall superheat with an increase in the heat flux, with a linear trend after the onset of nucleate boiling in the heat sink setup with single-channel manifold which occurs at a wall super heat of 5°C. The single-channel manifold heat sink setup also shows a jump in both the heat flux and wall superheat at a wall superheat of 15°C indicating a slight jump in performance because of the bubbles being generated increasing in size and detaching from the microchannels taking away more heat from the source. The highest heat flux achieved was 169.3 W/m^2 at a wall superheat of 24.3°C.

Discussing the effect of volumetric air quality on the flow-boiling phenomenon of the single-channel manifold heat sink apparatus, the changes in both heat flux and wall superheat when the volumetric quality changes from 0 to 0.8 is within the margin of error. This will be discussed more when comparing the single-channel manifold and manifold heat sink setup at specific voltages.

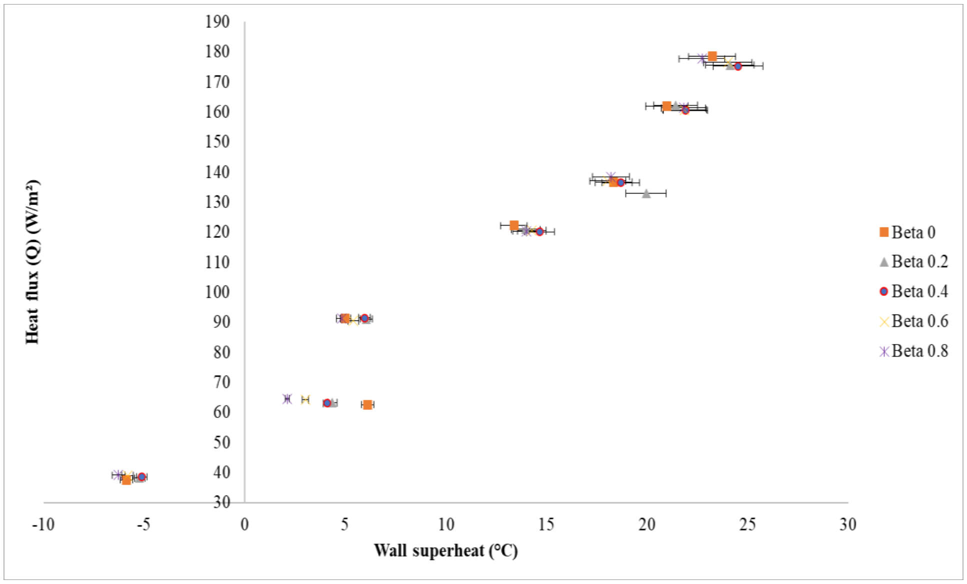

Figure 4-2: Plot showing the wall superheat as a function of heat flux for multi-channel manifold microchannel heat sink setup.

For the manifold heat sink apparatus, the results shown in Figure 4-2 indicate a similar trend as was seen in Figure 4-1 for the single-channel manifold heat sink setup. The same experiment conducted at a water flow rate of 6 GPH further validates the results obtained and discussed in this section. There is a jump in the heat flux at a wall superheat of 5° where the heat flux increases from around 63 W/cm^2 to 90 W/cm^2 which could indicate that this might be then onset of nucleate boiling and after that the trend followed by both the single-channel manifold and manifold heat sink are similar in the flow-boiling regime. The manifold configuration performs better overall with lower wall superheat than the configuration without manifold while providing better heat flux meaning the manifold configuration for a heat sink of this size is feasible when used for flow-boiling.

Similar to the results from the single-channel manifold configuration, the multi-channel manifold configuration also established that the effect of volumetric flow quality on the flow-boiling experiment was within the margin of error with the only outlier being the second lowest heat flux data indicating that a higher β (β = 0.6, 0.8) can provide the same heat flux performance at a lower wall superheat but since there is no onset of flow-boiling in this range of wall superheat, it could be considered insignificant but this anomaly could spark its own research in the future.

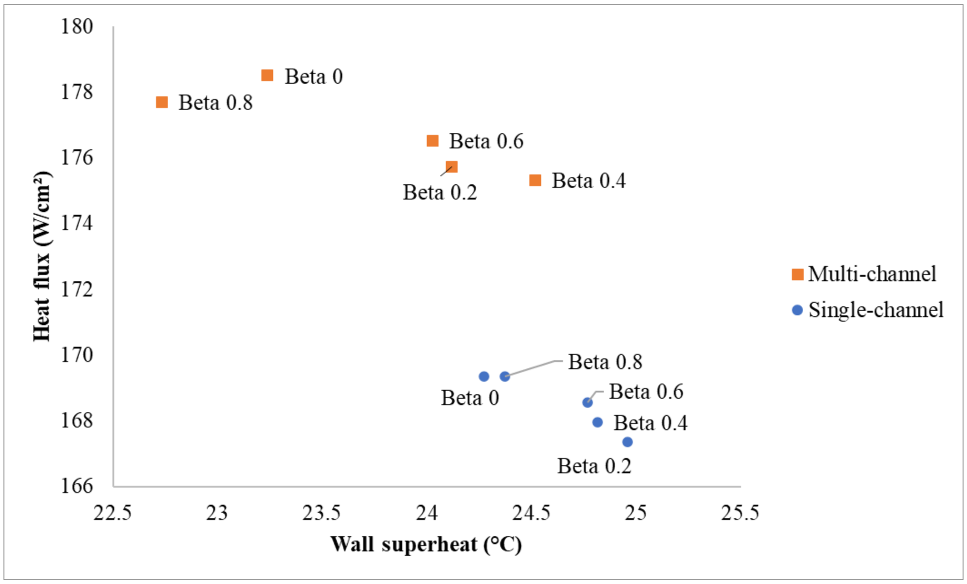

Figure 4-3: Comparison of the performance for single-channel and multi-channel manifold configurations at an average voltage of 46.834 V.

Figure 4-3 shows the performance increase for the heat sink configuration when multi-manifolds are introduced to the setup with an 8% increase in the heat flux while the temperature decreased by 6% conforming to literature published by other researchers comparing manifold MCHS with plain MCHS. The reason the performance increase is not as significant as the literature could have something to do with the fact that literature generally use a flat configuration for the plain surface on top of the heatsink while the single-channel manifold configuration manufactured by Bykski has one set of manifold for the fluid to move around increasing the convective surface area.

Furthermore, elaborating on the results discussed from Figure 4-1 and Figure 4-2, also shows that the effect of volumetric flow quality (β) on the wall superheat is within the margin of error . Something to note is that the performance for when no air is added is quite similar to when β is 0.8 while all the other β perform worse. Although within the margin of error, this result still indicates that adding air (and adding 80% air, 20% water) at most equals the performance for when there is no air added to the flow-boiling experiment.

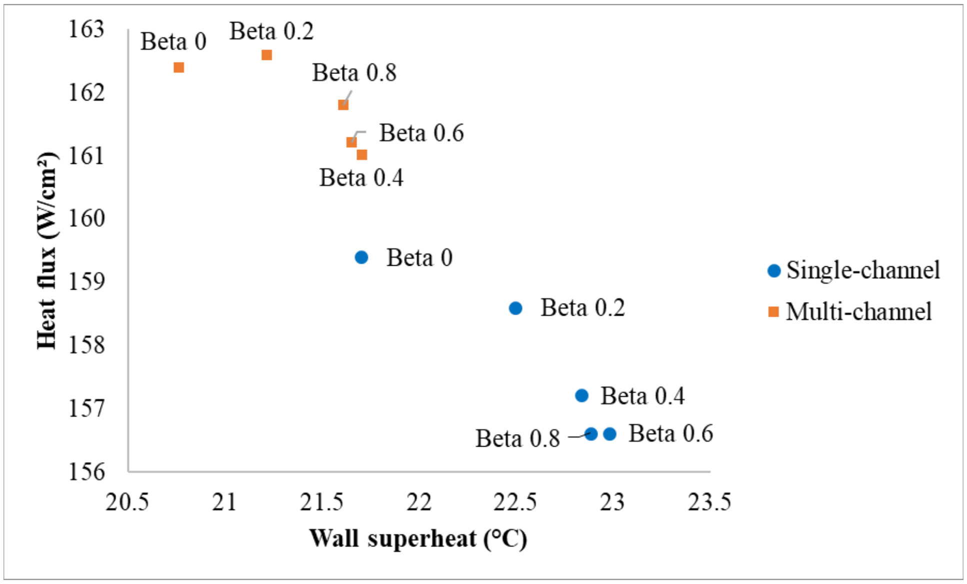

Figure 4-4: Comparison of the performance for single and multi-channel manifold configurations at a measured average voltage of 44.785 V

A similar trend can be seen when the voltage measured is 44.785 V where the manifold performs better for all β values by 2% in the heat flux criteria and more importantly, the multi-channel manifold performs 5% better than the single-channel manifold configuration at β = 0 with similar trends for other volumetric quality values. This decrease in wall superheat when more manifolds are introduced is significant in proving that the designed manifold setup performs better than the original setup with only a single set of manifolds purchased from manufacturer Bykski. Furthermore, Figure 4-4 also shows that adding no air to the flow-boiling experiment performs the best with β = 0.2 performing relatively closer to β = 0 which is a contrast from when the voltage being supplied was an average of 46.834 V.

Looking at the comparison between the single and multi-channel manifold configuration when there is no air being supplied, the performance from the multi-channel manifold configuration only starts outperforming the single-channel manifold configuration after the onset of flow-boiling as can be seen in Figure 4-5.

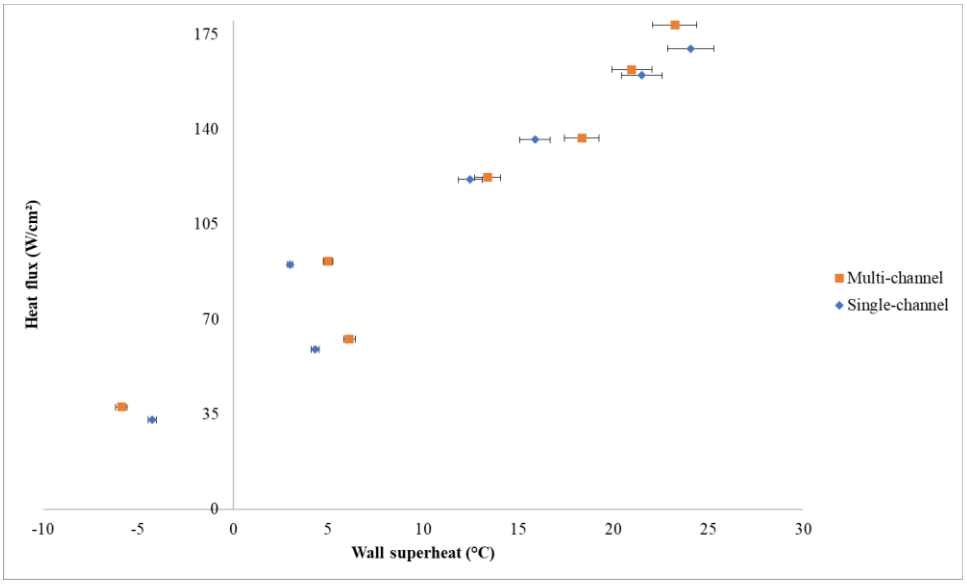

Figure 4-5: Performance comparison between single-channel manifold and multi-channel manifold configurations at β = 0.

The single-channel manifold configuration performs slightly better before the flow-boiling occurs at higher voltages which is apparent by the lower wall superheat highlighted in blue in the figure above but the interesting thing to note is that the heat flux remains almost identical which could mean that the configuration with single-channel manifold can absorb equal amount of heat compared to the multi-channel manifold configuration while maintaining lower heatsink base temperature.

Similarly, at β = 0, the trend continues with the single-channel manifold configuration outperforming the multi-channel manifold configuration before flow-boiling occurs, but the change in heat flux and wall superheat at higher voltages is even more pronounced than at β = 0 which is indicated by the rightmost two data points. One interesting thing of note from Figure 4-6 is that the multi-channel manifold outperforms at the second lowest data point value which is an anomaly.

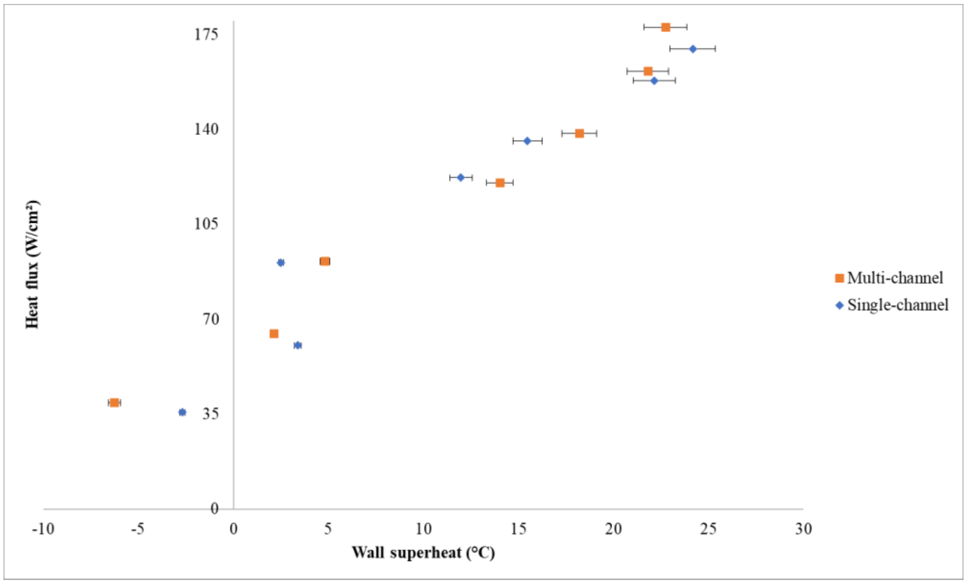

Figure 4-6: Performance comparison between the single-channel manifold and multi-channel manifold configuration at β = 0.8.

Following the results, a few images to visualize flow boiling were taken to show how the flow pattern was from β = 0 to β = 0.8.

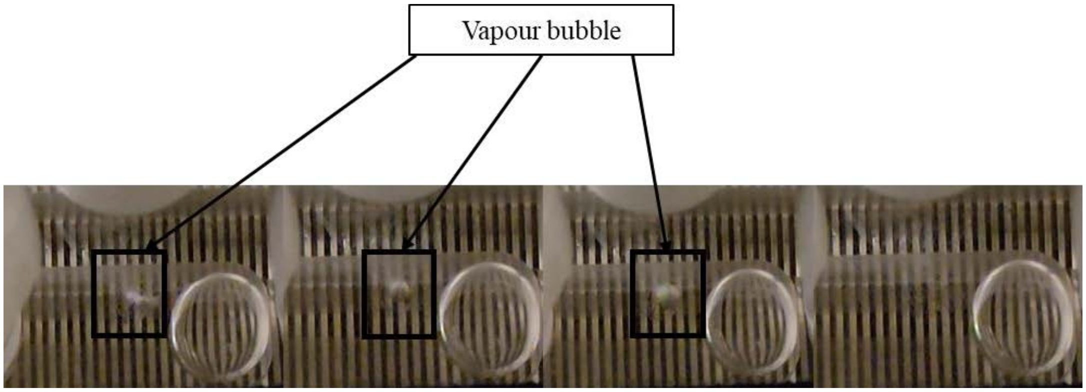

Figure 4-7: Onset of flow-boiling in MCHS configuration without manifolds at β = 0, average voltage measured of 33.746 V.

Figure 4-7 shows the onset of flow-boiling in the configuration with single-channel manifold when no air is added into the apparatus. This occurred at a measured voltage of 33.746 V and going over the image from left to right, it can be seen that sparse vapors movement occurs with only a single bubble forming in the channels and eventually rising to the surface after growing in size after which the bubble collapses.

Figure 4-8: Visualization of flow boiling in single-channel manifold MCHS configuration at β = 0, average voltage measured 44.785 V.

From Figure 4-8, when there is no air added, the bubbles exit the channels of the heat sink to the surface and coalesce into one giant bubble before it is pushed out by the oncoming flow of water. Flow-boiling is apparent, and the results show high heat flux at a relatively low wall superheat.

Figure 4-9: Flow-boiling visualization in MCHS configuration with single-channel manifold at β = 0 and average measured voltage of 41.842 V.

Similar to Figure 4-8, Figure 4-9 also visibly shows the bubbles forming and rising to the surface of the water block going on top of the heatsink and the bubble once again coalesce together before being pushed out by the oncoming flow.

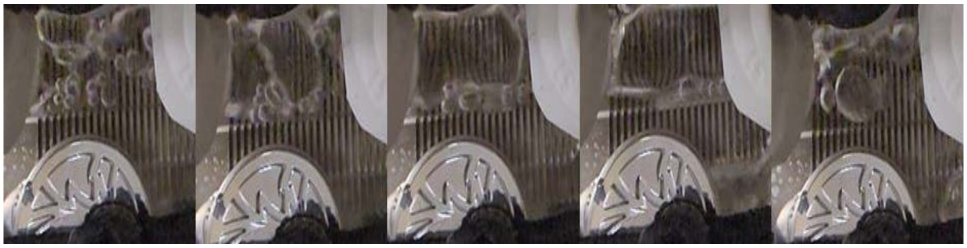

Figure 4-10: Flow-boiling visualization in MCHS configuration with single-channel manifold at β = 0.2 at 44.812 measured voltage.

Going over Figure 4-10 from left image to right, it can be seen that the flow pattern begins with vapors bubbles escaping from the channels to the surface which is pushed to the outlet by oncoming two phase fluid flow indicated by the growing bubbles which end at some point letting more vapors to escape from the channels for the cycle to repeat.

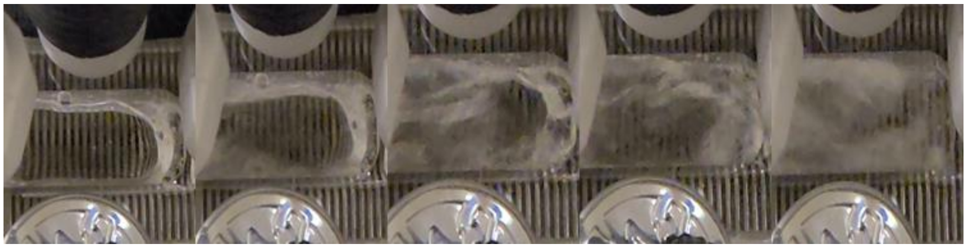

Figure 4-11: Flow-boiling visualization in MCHS configuration with single-channel manifold at higher β, 41.842 V measured voltage.

Figure 4-11 shows the flow-boiling phenomenon working in conjunction with an air-assistant flow where because the air flow rate is higher than the water flow rate, the fluid flow appears turbulent, and the flow comes in waves instead of as a single laminar flow as seen in Figure 4-10. Bubble formation due to flow-boiling is also only visible on the sides of the heat sink but not on the microchannels itself contrary to the phenomenon being observed in lower β flows.

4.3 Results for flow-boiling at water flow rate of 6 GPH

Similar to the results for a water flow rate of 10 GPH, a table figuring out the air flow rate based on the volumetric quality was required. Table 4-3 shows the calculated air flow rate required at different volumetric quality when the water flow rate is 6 GPM.

Table 4-3: Volumetric air quality when water flow rate is 6 GPH.

	0.1	0.2	0.3	0.4	0.5	0.6	0.7	0.8	0.9
Water Flow Rate (gph)	6	6	6	6	6	6	6	6	6
Air Flow Rate (gph)	0.67	1.50	2.57	4.00	6.00	9.00	14.00	24.00	54.00
Air flow rate (mLpm)	42.06	94.64	162.23	252.36	378.54	567.81	883.26	1514.16	3406.86

With the help of this table, the water flow rate was kept constant, and the air flow rate was once again modified based on the volumetric quality required during experimentation using the Omega air mass flow controllers and a few results were extrapolated.

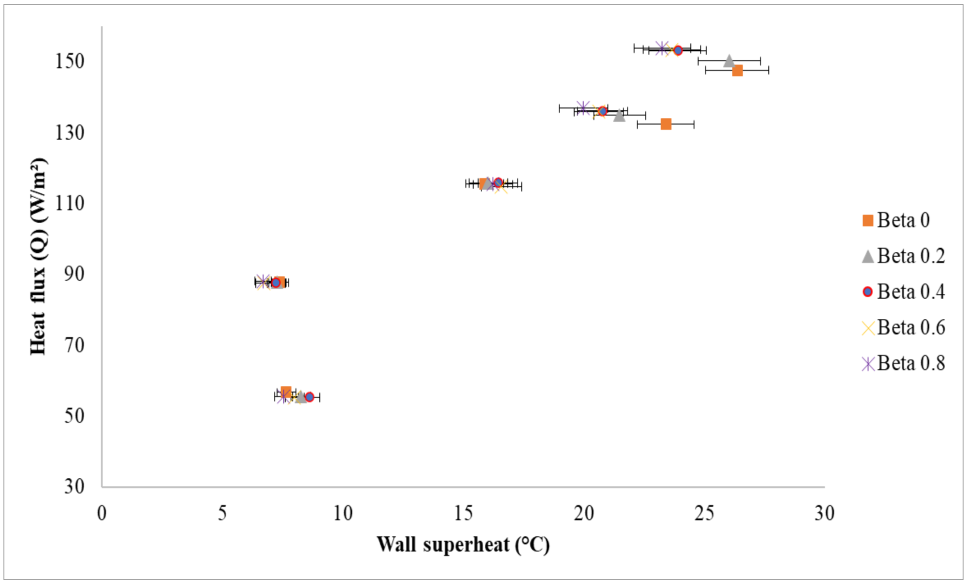

Figure 4-12: Plot showing the wall superheat as a function of heat flux for single-channel manifold microchannel heat sink setup at 6 GPH water flow rate.

Similar to Figure 4-1, Figure 4-12 shows a similar trend of increasing heat flux with an increase in the wall superheat of the heat sink. CHF was not obtained during experimentation and the plot shows the onset of flow boiling at a heat flux of 90 W/cm² since there is an increase in heat flux from the previous data point while maintaining a decrease in the wall superheat.

Addition of air to the experiment did not provide any meaningful increase in heat flux or a decrease in wall superheat as was the case during the experiments run at 10 GPH water flow rate which is further demonstrated when the manifolds are also introduced to the experiment.

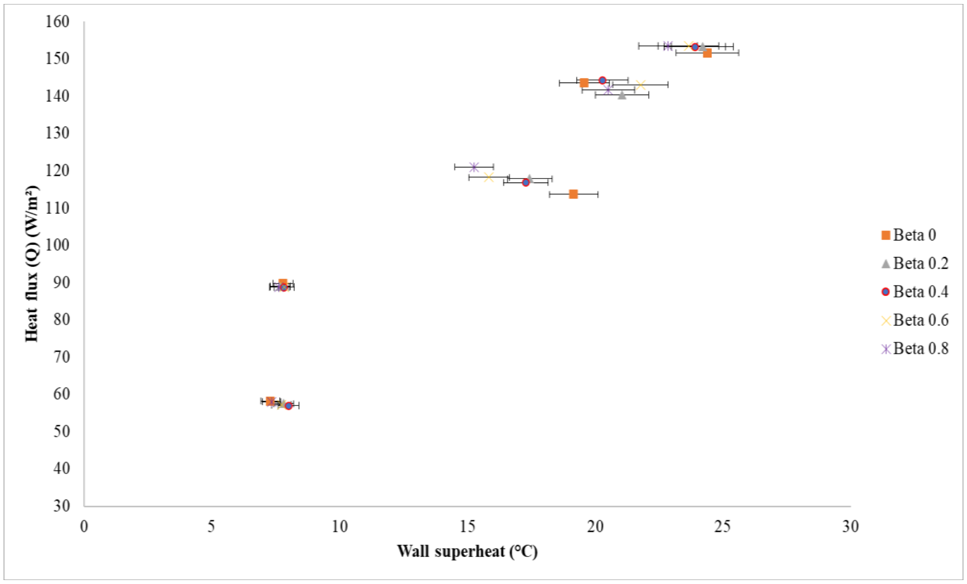

Figure 4-13: Plot showing the wall superheat as a function of heat flux for multi-channel manifold microchannel heat sink setup at 6 GPH water flow rate.

Similar to Figure 4-2, at the onset of flow boiling at around 90 W/cm², there is a sharp increase in heat flux while maintaining around the same wall superheat accounting for a 5% error in the values indicated by the error bars. There is a steady increase from there on out till the next data point around the 110-120 W/cm² heat flux and the trend of the steady increase remains the same. No CHF is achieved during experimentation with the manifold setup either.

Following the trend with the all the setups discussed so far, the air-assistant flow has little to no effect on the heat flux while only having minimal effect on the wall superheat almost all of which lie in the 5% error bar indicated in Figure 4-13 with the only exception being Beta 0 at the third data set which remains an outlier.

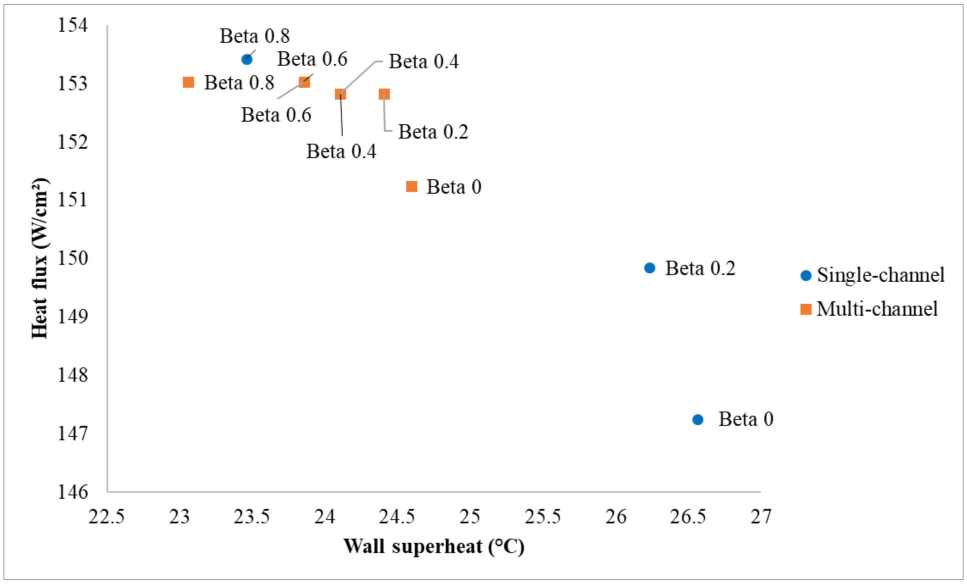

Figure 4-14: Comparison of the performance for manifold and single-channel manifold configurations at 42.875 V measured voltage at 6 GPH.

Figure 4-14 shows a comparison between the single and multi-channel manifold configuration at an average measured voltage of 42.875 V when the water flow rate if 6 GPH and the results shows that β at 0 and 0.2 perform the worst in the configuration with single-channel manifold lagging far behind all the other air-assistant counterparts. The other thing of note is that while the manifold setup performs the best, the performance increase is marginal.

One more thing of note is the jump in heat flux and a decrease in wall superheat when adding air to the single-channel manifold setup as seen in Figure 4-14, which could be an outlier as this phenomenon was not observed when comparing multi-channel manifold configuration with the single-channel manifold setup at a water flow rate of 10 GPH.

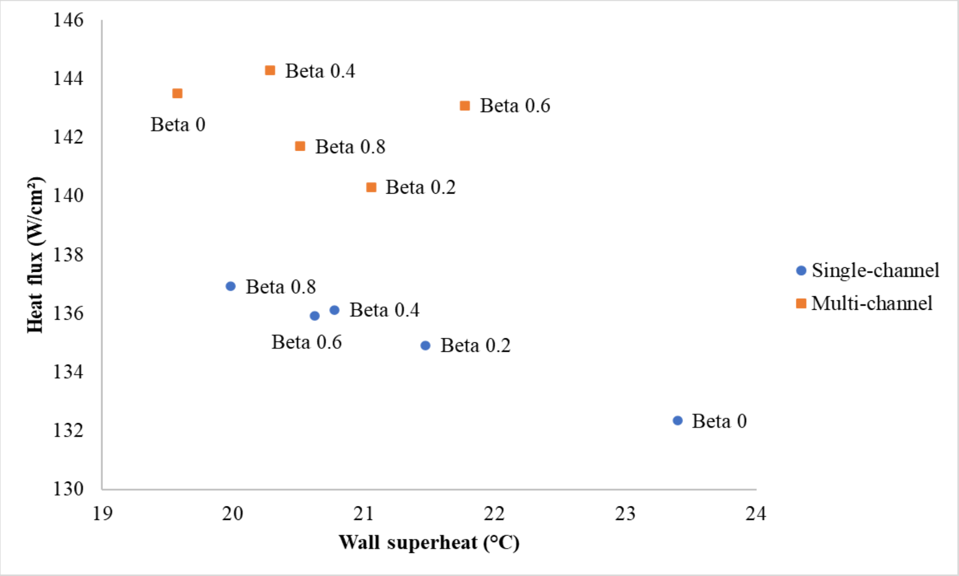

Figure 4-15: Comparison of the performance for manifold and single-channel manifold configurations at 41.725 V average measured voltage at 6 GPH.

Figure 4-15 shows that the multi-channel manifold configuration performs better than the setup with single-channel manifold in terms of heat flux with consistently higher heat flux at all volumetric air qualities at almost the same wall superheat. This indicates that the multi-channel manifold setup is better than the single-channel manifold setup at 6 GPH water flow rate like the results indicated when the water flow rate was 10 GPH.

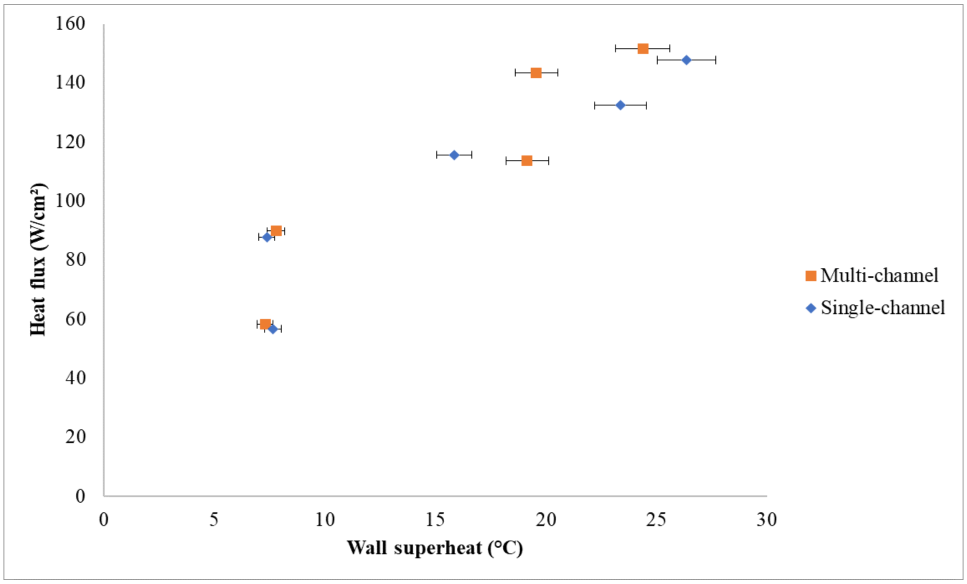

Figure 4-16: Performance comparison between the single-channel manifold and manifold configuration at β = 0 at 6 GPH.

Looking at the performance of the single and multi-channel manifold configuration at β = 0, the multi-channel manifold configuration performs better as expected in all, but one data point as seen in Figure 4-16. At the last two data points, both the wall superheat and the heat flux are better than the single-channel manifold configuration when air is not added validating the fact that the manifold does in fact uplift the performance of the microchannel heat sink.

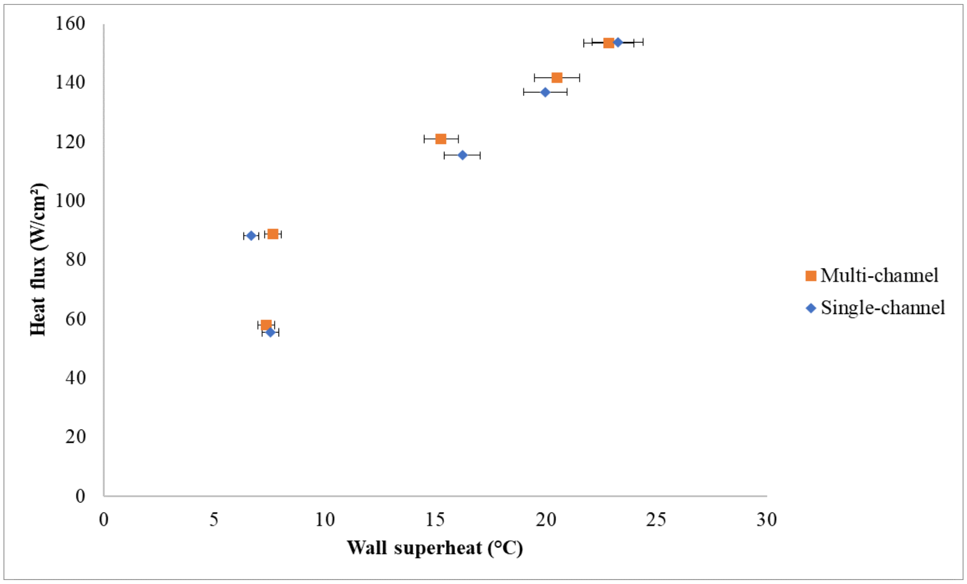

Figure 4-17: Performance comparison between the plain and manifold configuration at β = 0.8 at 6 GPH.

Looking at the performance for both single-channel manifold and manifold configuration across all heat fluxes when β = 0.8, Figure 4-17 indicates that the manifold configuration performs marginally better than the setup without manifolds which was expected. While the temperatures are identical or better on the setup without manifolds accounting for the 5% error bars, the heat flux is still better on the manifold configuration. The addition of air cuts down on the performance increase from the inclusion of more manifolds especially for the last two data points on the far right, meaning that the addition of air is actually worsening performance in this instance.

4.4 Comparison of the trend between 10 GPH and 6 GPH water flow rate

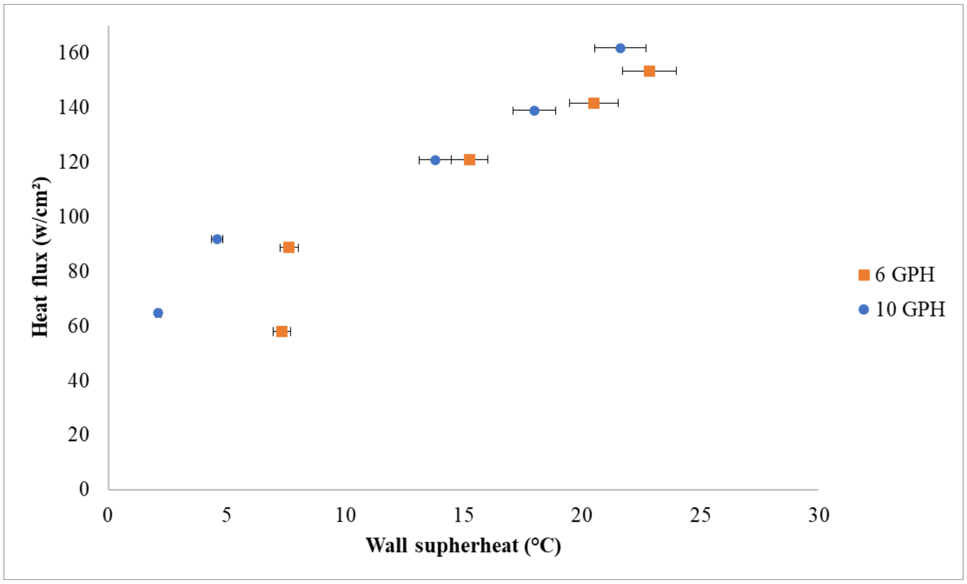

Figure 4-18: Comparison of trend between the 6 GPH and 10 GPH water flow rate at β = 0.8 for multi-channel manifold configuration.

Figure 4-18 shows the similarity of the trend between the two water flow rates at the highest β while also clarifying that flow rate does influence the heat transfer capabilities of the heat sink as there is an obvious change in the heat flux and the wall superheat with an increase in the flow rate. The increase in heat flux while subtle does not change the fact that the wall superheat is decreasing drastically before the onset of flow boiling and even after ONB, the decrease in the wall superheat is evident.

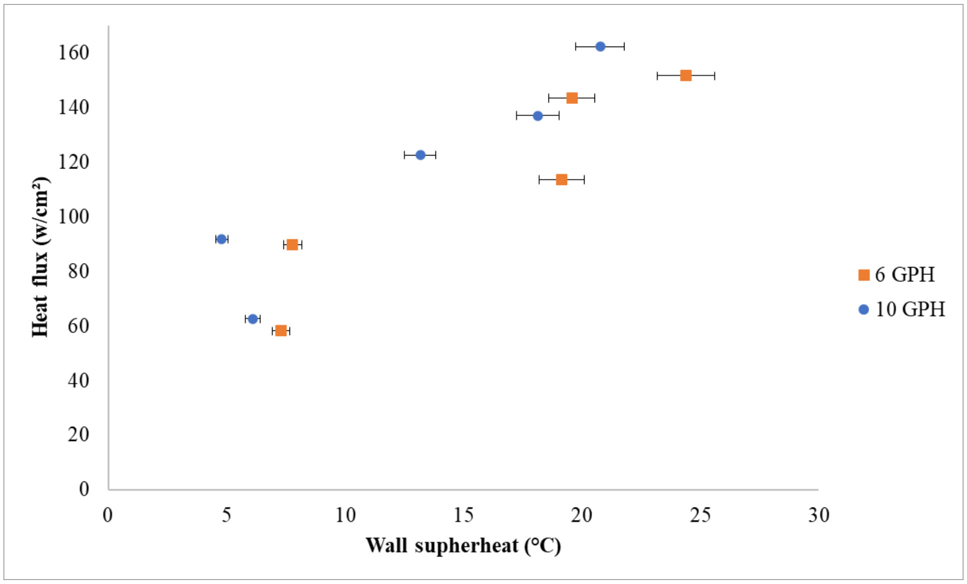

Figure 4-19: Comparison of trend between the 6 GPH and 10 GPH water flow rate at β = 0 for multi-channel manifold configuration.

Figure 4-19 has a similar trend for both flow rates of water when using the manifold configuration again showing the effect of flow rate on the ability to increase heat transfer performance. The difference between the two flow rates in terms of wall superheat is not as drastic as compared to the case with a higher volumetric quality indicated by the two leftmost data points.

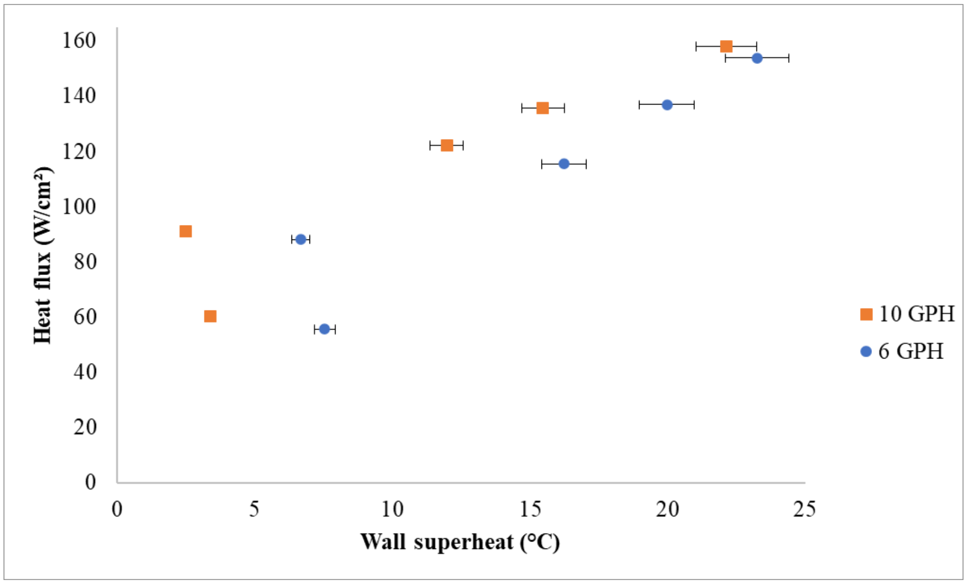

Figure 4-20: Comparison of trend between the 6 GPH and 10 GPH water flow rate at β = 0.8 for single-channel manifold configuration.

Figure 4-20 shows the effect of water flow rate when using the configuration with single-channel manifold and at the highest volumetric quality where again it is visible that an increase of flow rate of water causes the heat sink to perform better in all instances. The trend followed is similar with the only difference being the dramatic decrease in the wall superheat while maintaining a visible increase in the heat flux.

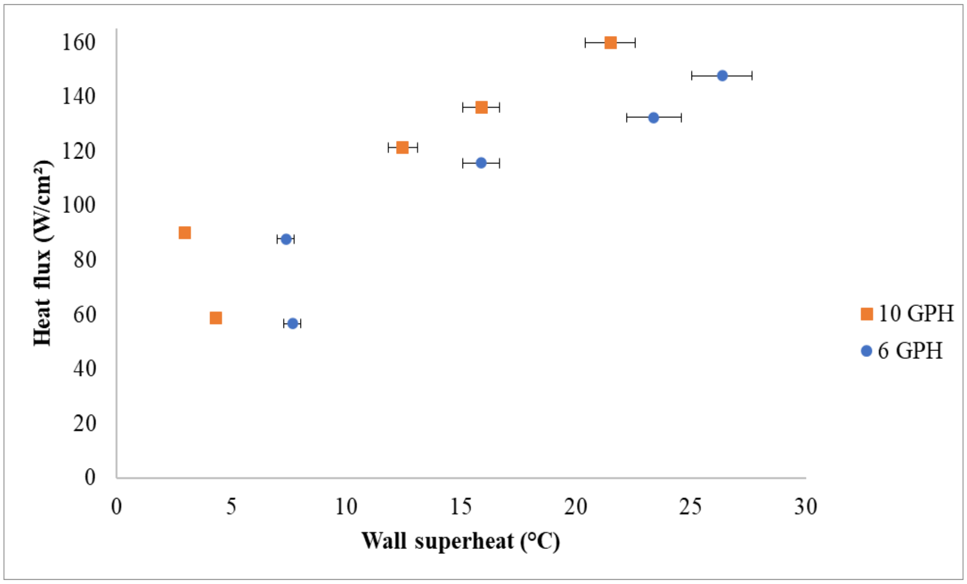

Figure 4-21: Comparison of trend between the 6 GPH and 10 GPH water flow rate at β = 0 for single-channel manifold configuration.

Figure 4-21 continues the trend where the higher flow rate of water yields higher heat fluxes as well as lower wall superheat when there is no addition of air. There is a visible difference in the wall superheat before the onset of flow boiling while maintaining a higher heat flux, but without the addition of air, it is noticeable that the last data point where the voltage supplied is the highest for both water flow rates maintains a much higher heat flux at a lower wall superheat for the 10 GPH case when compared to the experiment where the volumetric fraction β was 0.8.

5 Conclusion and Possible Future Work

5.1 Summary of Conclusion

This research was conducted in hopes of breaking new grounds when it comes to flow-boiling. The experiments conducted were conducted successfully and a new parameter in flow-boiling was incorporated. Though the results from the experiments were not as favorable as expected, this experiment still provided a few key insights on the interaction of manifold microchannel heat sink with air-assistant flow boiling.

1 The flow-boiling curve seen from both the 10 GPH and 6 GPH water flow rate experiments indicated that the multi-channel manifold configuration performed better than its single-channel manifold counterpart from manufacturer Bykski which follows what has been documented in literature namely from prominent figures in the field of flow boiling [6], [11], [30], [31] While the heat transfer enhancement is not as drastic as some of the results in those cited papers, presumably due to the inclusion of a single-channel already from the original water block shipped with the heat sink, multi-channel manifolds are still a better performer because of its ability to limit pressure drop, backflow of fluid, and overall providence of higher surface area compared to the single-channel manifold configuration from the manufacturer Bykski.

2 The addition of air to incorporate two phase fluid flow similar to the setup Rouse [1] had yielded no meaningful results when the impingement was confined to a microchannel heat sink. There were some instances where the air-assistant flow was close to a flow with no addition of air in terms of results, but most of the results showed that both the heat flux and the wall superheat were changing within the error specified for the experimental analysis.

3 Conducting the experiments for two different flow rates also showed that with an increase in water flow rate comes an increase in the performance which was expected according to literature. More fluid flow results in more heat transfer performance for both the multi-channel and single-channel manifold configurations.

6 References

[1] V. J. Rouse, “Comparison of heat transfer and fluid flow characteristics between submerged and free surface jet impingement for two-phase flow,” 2018.

[2] W. A. Bevan, “An Experimental Study of Porous Mediums on Heat Transfer Characteristics Subjected to Water Jet Impingement,” 2022.

[3] D. B. Tuckerman and R. F. W. Pease, “High-Performance Heat Sinking for VLSI,” *IEEE Electron Device Letters*, vol. EDL-2, no. 5, 1981, doi: 10.1109/EDL.1981.25367.

[4] S. G. Kandlikar and W. J. Grande, “Evaluation of single phase flow in microchannels for high heat flux chip cooling-thermohydraulic performance enhancement and fabrication technology,” *Heat Transfer Engineering*, vol. 25, no. 8. 2004. doi: 10.1080/01457630490519772.

[5] Y. A. Cengel, *Heat and mass transfer : fundamentals & applications / Yunus A. Çengel, Afshin J. Ghajar*. 2015.

[6] A. Kalani and S. G. Kandlikar, “Evaluation of pressure drop performance during enhanced flow boiling in open microchannels with tapered manifolds,” *J Heat Transfer*, vol. 136, no. 5, May 2014, doi: 10.1115/1.4026306.

[7] S. Nukiyama, “The maximum and minimum values of the heat Q transmitted from metal to boiling water under atmospheric pressure,” *Int J Heat Mass Transf*, vol. 9, no. 12, 1966, doi: 10.1016/0017-9310(66)90138-4.

[8] S. NUKIYAMA, “The Maximum and Minimum Values of the Heat Q Transmitted from Metal to Boiling Water under Atmospheric Pressure,” *Journal of the Society of Mechanical Engineers*, vol. 37, no. 206, 1934, doi: 10.1299/jsmemagazine.37.206_367.

[9] E. Galvis, “Single-Phase and Boiling Flow in Microchannels with High Heat Flux,” 2012.

[10] T. Harirchian and S. V. Garimella, “Effects of channel dimension, heat flux, and mass flux on flow boiling regimes in microchannels,” *International Journal of Multiphase Flow*, vol. 35, no. 4, 2009, doi: 10.1016/j.ijmultiphaseflow.2009.01.003.

[11] W. Qu and I. Mudawar, “Flow boiling heat transfer in two-phase micro-channel heat sinks-I. Experimental investigation and assessment of correlation methods,” *Int J Heat Mass Transf*, vol. 46, no. 15, pp. 2755–2771, Jul. 2003, doi: 10.1016/S0017-9310(03)00041-3.

[12] A. Kalani, “Flow Boiling Heat Transfer Over Open Microchannels With Flow Boiling Heat Transfer Over Open Microchannels With Tapered Manifold Tapered Manifold,” 2016. [Online]. Available: https://scholarworks.rit.edu/theses

[13] W. K. Kuan and S. G. Kandlikar, “Experimental study on the effect of stabilization on flow boiling heat transfer in microchannels,” in *Proceedings of the 4th International Conference on Nanochannels, Microchannels and Minichannels, ICNMM2006*, 2006. doi: 10.1115/icnmm2006-96045.

[14] A. Mukherjee and S. G. Kandlikar, “The effect of inlet constriction on bubble growth during flow boiling in microchannels,” *Int J Heat Mass Transf*, vol. 52, no. 21–22, 2009, doi: 10.1016/j.ijheatmasstransfer.2009.04.025.

[15] G. M. Harpole and J. E. Eninger, “Micro-channel heat exchanger optimization,” in *Proceedings - IEEE Semiconductor Thermal and Temperature Measurement Symposium*, 1991. doi: 10.1109/stherm.1991.152913.

[16] D. Kong *et al.*, “A holistic approach to thermal-hydraulic design of 3D manifold microchannel heat sinks for energy-efficient cooling,” *Case Studies in Thermal Engineering*, vol. 28, 2021, doi: 10.1016/j.csite.2021.101583.

[17] D. Fontanarosa, L. Francioso, M. G. De Giorgi, and M. R. Vetrano, “Mems vaporazing liquid microthruster: A comprehensive review,” *Applied Sciences (Switzerland)*, vol. 11, no. 19. 2021. doi: 10.3390/app11198954.

[18] D. A. Zumbrunnen and M. Balasubramanian, “Convective heat transfer enhancement due to gas injection into an impinging liquid jet,” *J Heat Transfer*, vol. 117, no. 4, 1995, doi: 10.1115/1.2836275.

[19] A. Serizawa, O. Takahashi, Z. Kawara, T. Komeyama, and I. Michiyoshi, “HEAT TRANSFER AUGMENTATION BY TWO-PHASE BUBBLY FLOW IMPINGING JET WITH A CONFINING WALL,” 2019. doi: 10.1615/ihtc9.1360.

[20] B. K. Friedrich, A. W. Glaspell, and K. Choo, “The effect of volumetric quality on heat transfer and fluid flow characteristics of air-assistant jet impingement,” *Int J Heat Mass Transf*, vol. 101, 2016, doi: 10.1016/j.ijheatmasstransfer.2016.05.021.

[21] S. G. Kandlikar, T. Widger, A. Kalani, and V. Mejia, “Enhanced flow boiling over open microchannels with uniform and tapered gap manifolds,” *J Heat Transfer*, vol. 135, no. 6, 2013, doi: 10.1115/1.4023574.

[22] R. S. Andhare, A. Shooshtari, S. V. Dessiatoun, and M. M. Ohadi, “Heat transfer and pressure drop characteristics of a flat plate manifold microchannel heat exchanger in counter flow configuration,” *Appl Therm Eng*, vol. 96, 2016, doi: 10.1016/j.applthermaleng.2015.10.133.

[23] Y. Peng, Z. Li, S. Li, B. Cao, X. Wu, and X. Zhao, “The experimental study of the heat ransfer performance of a zigzag-serpentine microchannel heat sink,” *International Journal of Thermal Sciences*, vol. 163, 2021, doi: 10.1016/j.ijthermalsci.2021.106831.

[24] F. Battaglia, F. Singer, D. C. Deisenroth, and M. M. Ohadi, “Experimental characterization of two-phase cooling of power electronics in thermosiphon and forced convection modes,” *Journal of Electronic Packaging, Transactions of the ASME*, vol. 143, no. 3, 2021, doi: 10.1115/1.4049564.

[25] W. Escher, T. Brunschwiler, B. Michel, and D. Poulikakos, “Experimental investigation of an ultrathin manifold microchannel heat sink for liquid-cooled chips,” *J Heat Transfer*, vol. 132, no. 8, 2010, doi: 10.1115/1.4001306.

[26] K. P. Drummond *et al.*, “Characterization of hierarchical manifold microchannel heat sink arrays under simultaneous background and hotspot heating conditions,” *Int J Heat Mass Transf*, vol. 126, 2018, doi: 10.1016/j.ijheatmasstransfer.2018.05.127.

[27] K. W. Jung *et al.*, “Embedded cooling with 3D manifold for vehicle power electronics application: Single-phase thermal-fluid performance,” *Int J Heat Mass Transf*, vol. 130, 2019, doi: 10.1016/j.ijheatmasstransfer.2018.10.108.

[28] X. Zhang, R. Tiwari, A. H. Shooshtari, and M. M. Ohadi, “An additively manufactured metallic manifold-microchannel heat exchanger for high temperature applications,” *Appl Therm Eng*, vol. 143, 2018, doi: 10.1016/j.applthermaleng.2018.08.032.

[29] S. Moldovan, “Measurement Errors and Uncertainty Analysis.”

[30] D. Liu and S. V. Garimella, “Flow boiling heat transfer in microchannels,” *J Heat Transfer*, vol. 129, no. 10, 2007, doi: 10.1115/1.2754944.

[31] P. K. B. Rego, “Flow Boiling in Open Microchannels with Tapered Manifolds using Flow Boiling in Open Microchannels with Tapered Manifolds using Ethanol in a Gravity-Driven Flow Ethanol in a Gravity-Driven Flow.” [Online]. Available: https://scholarworks.rit.edu/theses

7 Appendix

Appendix – A: Preparation of a heat resistant mount for heat sink setup

To linearize the experiment for both the single-channel manifold and the manifold configuration to make sure the heat sink was placed on top of the heat source at the exact same position every time, a fitting made from temperature resistant resin was modelled and manufactured. The first step in creating this fitting was to make a model based on the top part of the assembled heater apparatus as seen in Figure 3-11. The top surface with all the hole diameter and distances were measured along with the base of the heat sink which was then used to model the top fitting which can be seen in Figure 7-1.

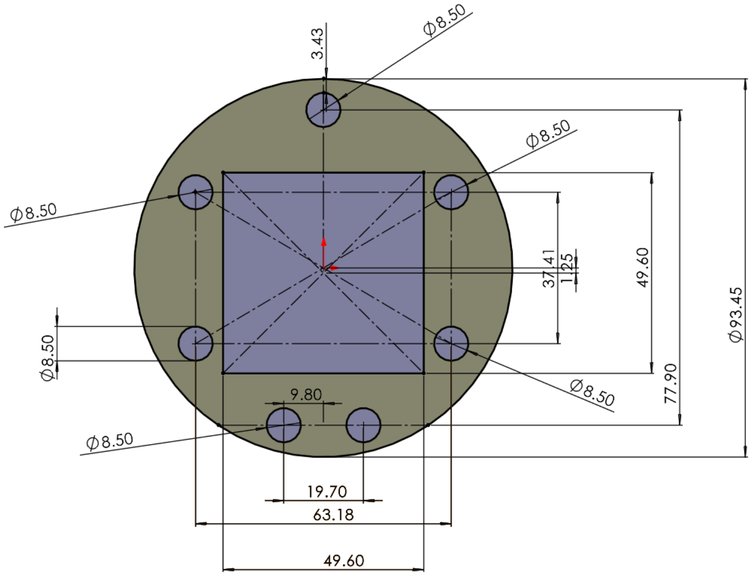

Figure 7-1: Top cover dimensions on SolidWorks.

After the dimensions were taken, a PRUSA 3D printer was used to make a prototype as seen in Figure 7-2. This made sure that a final design could be printed using flexible 3D printed resin so that it doesn't bend or break during experiments when the heater setup reaches high temperatures.

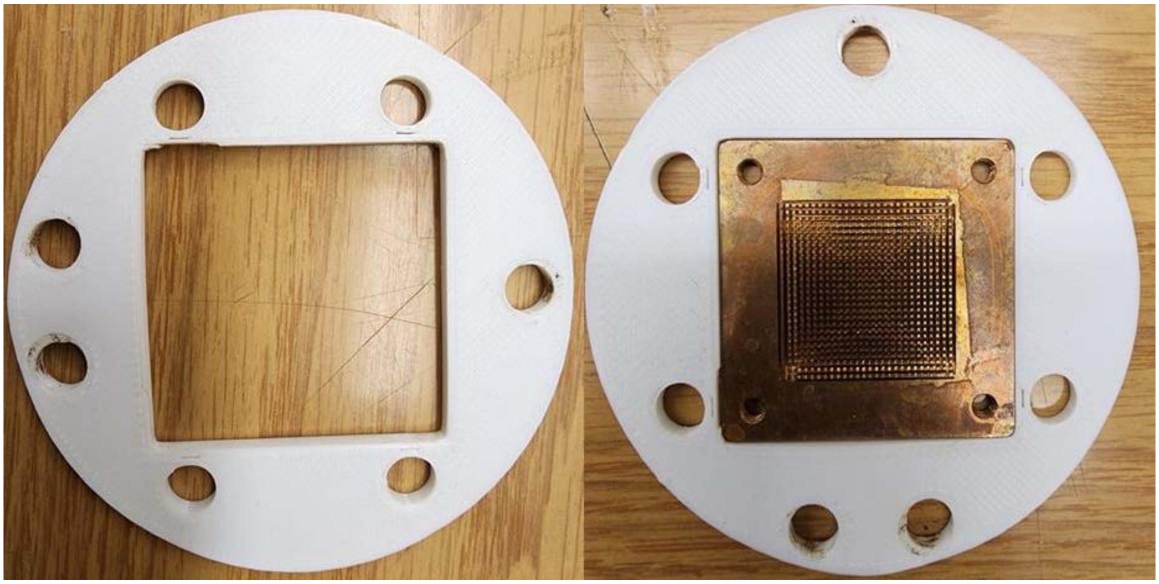

Figure 7-2: Initial prototype using PLA to examine the fit.

The final 3D printed resin made from heat resistant material which could withstand up to 210°C according to FormLabs' website can be seen in Figure 7-3 along with the fit on the heat sink used for experiments.

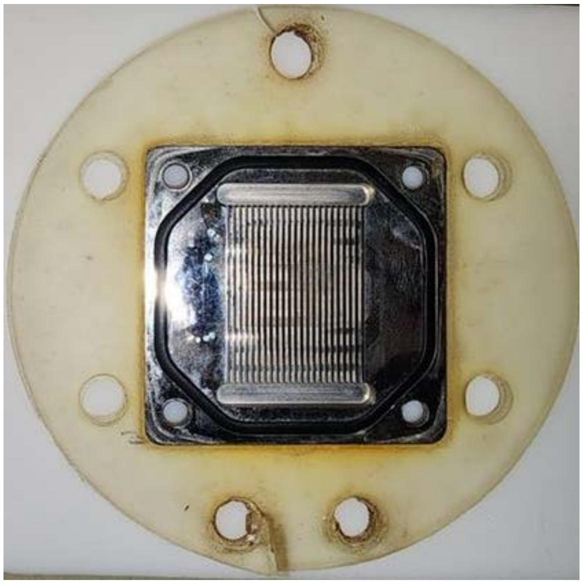

Figure 7-3: Final flexible resin print along with the heat sink used to show the fit.

Appendix – B: Propagation of error derivation

The derivation for the uncertainty of each of the measured quantities discussed in Section 4.3 is shown below.

7.1.1 Heat Flux Uncertainty Analysis

The equation for heat flux, determined using the two thermocouples inside the heat blocks, was calculated using equations (2) and (7) yielding a final equation as shown below:

$$q'' = \frac{k_{Cu}(T_1 - T_2)}{x} \tag{9}$$

The variables were then substituted to the error propagation equation (13) which gives:

$$e_{q''} = \sqrt{e_{T_1}^2 + e_{T_2}^2 + e_d^2} \tag{16}$$

Since thermal conductivity is a material property, it is considered to have no uncertainty associated with it. To find the relative uncertainty for temperatures for T_1 and T_2, equation (17) was used:

$$u_T = \sqrt{u_{precision}^2} \tag{17}$$

The precision error is based on the student-t distribution for N data points and a 95% probability multiplied with the standard deviation of the value measured by the data acquisition system. There are no other errors associated with the temperature as the bias error associated with the thermocouples were already factored into the temperatures being measured during experimentation which denoted the true temperature values for T_1 and T_2.

This total uncertainty for temperature (u_T) was then converted to the relative uncertainty being used in (16) by using equation (18)

$$e_T = \frac{u_T}{T} \tag{18}$$

This relative uncertainty applied for both T_1 and T_2 which completed the first two terms for the uncertainty associated with the heat flux. The third term which was the uncertainty associated with the distance measured between the two thermocouples was done using a digital caliper which had a resolution error of 0.01 mm. The total uncertainty of the distance between the thermocouple was given by equation (19):

$$u_d = \frac{1}{2}(res\ error) \tag{19}$$

This total uncertainty was again converted to relative uncertainty using equation (20)

$$e_d = -\frac{u_d}{d} \tag{20}$$

So, the final equation of relative uncertainty associated with the heat flux becomes:

$$e_{q''} = \sqrt{\left(\frac{u_{precision_{T_1}}}{T_1}\right)^2 + \left(\frac{u_{precision_{T_2}}}{T_2}\right)^2 + \left(-\frac{res\ error}{2d}\right)^2} \tag{15}$$

7.1.2 Surface Temperature Uncertainty Analysis

Similarly, the uncertainty associated with the temperature of the heat sink base was calculated by first analyzing the equation of the heat sink base temperature given in equation (10).

$$T_{hs_{base}} = T_1 - q'' A\, R_{tot} \tag{21}$$

The uncertainty associated with T_1 has already been calculated, so using the error propagation formula from equation (13), the uncertainty associated with the heat flux affecting the surface temperature of the heat sink was calculated as follows

$$e_{q^{''}} = \frac{1}{T_1 - R_{tot}q^{''}A}\frac{\partial}{\partial Q}\left(T_1 - R_{tot}q^{''}A\right)u_{q^{''}}$$

$$e_{q^{''}} = \frac{1}{T_1 - R_{tot}q^{''}A}\left(-R_{tot}\,A\right)u_{q^{''}} \tag{22}$$

Here, $u_{q^{''}}$ is the uncertainty associated with the heat flux, which would just be the relative uncertainty calculated for heat flux in equation (16).

Since, R_{tot} is a sum of the material properties, it is considered to have no uncertainty associated with it. Finally, for the uncertainty associated with the area of the heat sink:

$$e_A = \frac{1}{T_1 - R_{tot}q^{''}A}\frac{\partial}{\partial A}\left(T_1 - R_{tot}q^{''}A\right)u_A$$

$$e_A = \frac{1}{T_1 - R_{tot}q^{''}A}\left(-R_{tot}\,q^{''}\right)u_A \tag{23}$$

The uncertainty associated with area (u_A) is just the total uncertainty associated with the distance multiplied by the square root of 2 as the surface area was calculated by measuring the length and width of the top surface of the copper block using a digital caliper.

Then, the relative uncertainty associated with the surface temperature of the heat sink can be calculated using the square root of the sum of squares of all the uncertainties the surface temperature is dependent on yielding equation (12)

$$e_{T_{HS_{base}}} = \sqrt{e_{T_1}^2 + e_{q^{''}}^2 + e_A^2}$$

$$e_{T_{HS_{base}}} = \sqrt{\left(\frac{u_{precision_{T_1}}}{T_1}\right)^2 + \left(\frac{1}{T_1 - R_{tot}q^{''}A}\left(-R_{tot}\,A\right)\right)^2 u_{q^{''}}^2 + \left(\frac{1}{T_1 - R_{tot}q^{''}A}\left(-R_{tot}\,q^{''}\right)\right)^2 u_A^2} \tag{14}$$